Review

Suruj S. Deka*, Sizhu Jiang, Si Hui Pan and Yeshaiahu Fainman

Nanolaser arrays: toward application-driven dense integration

https://doi.org/10.1515/nanoph-2020-0372
Received July 4, 2020; accepted September 8, 2020; published online September 29, 2020

Abstract: The past two decades have seen widespread efforts being directed toward the development of nanoscale lasers. A plethora of studies on single such emitters have helped demonstrate their advantageous characteristics such as ultrasmall footprints, low power consumption, and room-temperature operation. Leveraging knowledge about single nanolasers, the next phase of nanolaser technology will be geared toward scaling up design to form arrays for important applications. In this review, we discuss recent progress on the development of such array architectures of nanolasers. We focus on valuable attributes and phenomena realized due to unique array designs that may help enable real-world, practical applications. Arrays consisting of exactly two nanolasers are first introduced since they can serve as a building block toward comprehending the behavior of larger lattices. These larger-sized lattices can be distinguished depending on whether or not their constituent elements are coupled to one another in some form. While uncoupled arrays are suitable for applications such as imaging, biosensing, and even cryptography, coupling in arrays allows control over many aspects of the emission behavior such as beam directionality, mode switching, and orbital angular momentum. We conclude by discussing some important future directions involving nanolaser arrays.

Keywords: applications; arrays; coupling; dynamics; integration; nanolasers.

1 Introduction

In the quest for attaining Moore's law-type scaling for photonics, miniaturization of components for dense integration is imperative [1]. One of these essential nanophotonic components for future photonic integrated circuits (PICs) is a chip-scale light source. To this end, the better part of the past two decades has seen the development of nanoscale lasers that offer salient advantages for dense integration such as ultracompact footprints, low thresholds, and room-temperature operation [2–4]. These nanolasers have been demonstrated based on a myriad of cavity designs and physical mechanisms some of which include photonic crystal nanolasers [5–8], metallo-dielectric nanolasers [9–15], coaxial-metal nanolasers [16, 17], and plasmonic lasers or spasers [18–22]. The applications of such ultrasmall lasers are not just limited to on-chip communications as their unique characteristics allow them to be used for biological sensing [7, 23, 24], super-resolution imaging [25, 26], as well as optical interconnects [27].

In most practical applications, however, a single nanolaser would never operate in isolation but rather in tandem with multiple such devices. Doing so can enable novel applications that would otherwise be infeasible to achieve using an isolated laser. Therefore, the next logical step in the evolution of nanolaser technology is to realize large-scale, dense arrays of nanolasers by leveraging the knowledge gained so far from the plethora of studies on single such emitters.

In this review, we focus on the progress made toward realizing nanolaser arrays. In Section 2, we elaborate on the interaction between only two nanolaser devices. Such a dual nanolaser system can be considered as a unit cell that can assist in understanding larger scale arrays. Section 3 discusses the distinct types of arrays demonstrated thus far and the unique applications they can help enable. Finally, we conclude and present possible research directions yet to be explored on this front in Section 4.

***Corresponding author: Suruj S. Deka**, Department of Electrical and Computer Engineering, University of California at San Diego, La Jolla, CA, 92093-0407, USA, E-mail: sdeka@eng.ucsd.edu
Sizhu Jiang, Si Hui Pan and Yeshaiahu Fainman, Department of Electrical and Computer Engineering, University of California at San Diego, La Jolla, CA, 92093-0407, USA

2 Interaction between two nanolasers

Perusing the recent literature on array architectures of nanolasers reveals that based on array size, most studies can be segmented into two categories. If N is used to denote the number of individual elements (or nanolasers) in the array, the categories correspond to the cases of $N = 2$ and $N > 2$. Prior to reviewing what occurs in larger arrays, it is helpful to first consider an array of only two resonant nanocavities (i.e., $N = 2$). The primary reason for this is that a dual nanolaser system can be regarded as a type of unit cell or building block that can help explain the behaviors observed in larger lattices. Since lasers are inherently nonlinear systems, the interactions between them can produce rich and complex dynamics. The linewidth enhancement factor for semiconductor materials used in most gain media further complicates the physics involved [28]. In this scenario, limiting the number of nanolasers to two simplifies the associated rate equations and can be a stepping-stone toward understanding array behaviors. This section reviews a few aspects of the interesting physics that can result from the interaction of two nanolasers.

2.1 Creation of supermodes

The coupling between two lasers can be introduced in various near-field and far-field manners including evanescent coupling [29–37], leaky wave coupling [38], and mutual injection [39]. Among them, evanescent coupling induced between two resonant cavities in close proximity is the most common and feasible way to build densely integrated nanolaser arrays and has already been extensively investigated in microscale cavities [29–34]. This type of coupling occurs when increased interaction between the evanescent electromagnetic fields of the two individual resonators gives rise to a characteristic splitting of the observed modes in both frequency and loss [29, 32–34]. The bifurcation is the consequence of the creation of bonding and antibonding supermodes which are dissimilar in both their optical losses and frequency.

With advances in fabrication technology, the corresponding higher precision has facilitated moving from the microscale to the nanoscale. Consequentially, similar coupling behavior has now been reported in coupled nanolaser cavities. Deka et al. demonstrate such coupling in a dual nanolaser system comprising two metallo-dielectric nanocavities shown in the schematic in Figure 1A [35]. In their design, the distance between the two resonators, represented by d in the schematic, is varied, while the modes supported by the system are recorded. The authors first consider two extreme cases of when the cavities are spaced far apart (d = 90 nm) and when their dielectric shields are in contact (d = 0 nm). For each case, the electric field intensity is calculated, as portrayed in a two-dimensional side and top cross section in Figure 1B. When designed far apart, the TE_{011} modes supported by the two equally sized nanocavities are independent and identical (Figure 1B, left). This results from the metal between the resonators damping any evanescent fields arising from the cavities, thus inhibiting coupling [35]. If d = 0 nm, however, the increased evanescent coupling between the cavities leads to the formation of two new modes – the antibonding supermode (Figure 1B, middle) and the bonding supermode (Figure 1B, right). The former exhibits strong confinement of the electromagnetic field to the individual gain media while the latter demonstrates an electric field maximum in the central region between the two gains due to constructive interference.

Furthermore, by varying d in discrete steps and calculating the eigenmode wavelength (λ) and quality factor (Q) of the cavity modes for each distance, the authors report a split in the two parameters as d is reduced (Figure 1C, top and middle). Since the cavities are purposed for lasing, the gain threshold, g_{th}, of each mode is also calculated (Figure 1C, bottom). Owing to a larger overlap with the dissipative metal, the bonding supermode experiences a higher loss and is therefore less likely to lase as evidenced by its higher threshold [35]. The creation of these dissimilar supermodes due to evanescent coupling has also been reported in other material systems such as photonic crystals. Figure 1D depicts a schematic of two coupled photonic crystal nanolasers taken from the work of Hamel et al. [36]. When pumped equally, their system supports bonding and antibonding supermodes with the latter becoming the dominant lasing mode at higher pump powers (Figure 1E). Therefore, the formation of bonding and antibonding supermodes is one of the most basic phenomena to occur due to increased evanescent coupling between nanolasers.

It is important to note, however, that besides bonding and antibonding modes, various other types of supermodes can also be observed in coupled nanolaser systems. Parto et al. [40] demonstrate that depending on the size of the metallic nanodisks used in their study, either ferromagnetic (FM) or antiferromagnetic (AF) coupling is exhibited between the constituent elements of the lattice. These FM and AF couplings arise due to the interaction between the vectorial electromagnetic modes supported by the nanocavities which exchange spin Hamiltonians like in

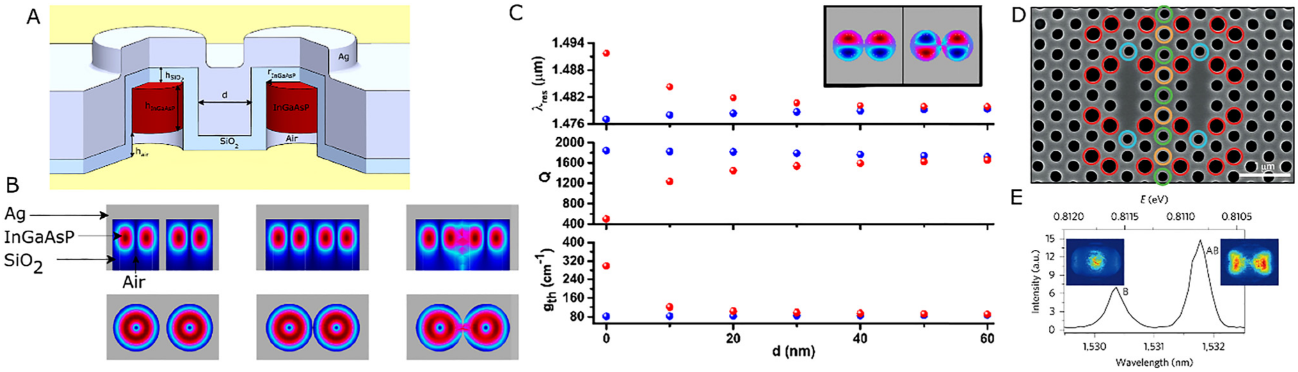

Figure 1: Supermode creation in dual nanolaser systems.
(A) Two coupled metallo-dielectric nanolasers, where the distance between cavities is represented by *d*. (B) Electric field intensity profiles across the side (top row) and top (bottom row) cross sections of the nanolaser system shown in (A). When $d = 90$ nm (left), system supports two identical and independent TE_{011} modes. When $d = 0$ nm, two new modes are supported by the system – antibonding (middle) and bonding supermodes (right). (C) Eigenmode wavelengths (λ), quality factors (Q), and gain thresholds (g_{th}) for the two modes supported by the dual nanolaser system at varying *d*. Inset: electric field distributions of the antibonding (left) and bonding (right) supermodes. (A), (B) and (C) reprinted from a study by Deka et al. [35] with permission. (D) Two coupled photonic crystal nanolasers and (E) the bonding (B, left peak) and antibonding (AB, right peak) modes supported in this design. (D) and (E) adapted and reprinted from a study by Hamel et al. [36] with permission.

magnetic materials [40, 41]. These recent results can help pave the path toward achieving ultracompact, on-chip photonic platforms that implement spin Hamiltonians for solving complex optimization problems [41].

2.2 Analysis of nonlinear dynamics

Besides supermodes creation, the coupling between two lasers can also produce rich nonlinear dynamics. Specifically, for the case of coupled nanolasers, a multitude of dynamical regimes including stable phase locking, periodic intensity oscillations, as well as chaotic fluctuations can be achieved that can help enable a wide variety of applications. For instance, coupled nanolasers operating in a stable phase locking manner are essential for building high power laser arrays [42, 43], whereas periodic oscillations may be used for on-chip modulation and radio frequency (RF) wave generation [44]. Recently, chaotic synchronization of nanolasers which can prove useful in quantum experiments for random number generation and secure key exchange has also garnered some attention [45]. Consequentially, analyzing the diverse dynamical regimes at play for two coupled nanolasers is of critical importance.

Investigation of dynamics usually involves solving the coupled rate equations and analyzing the dependence of the dynamical regimes observed on essential parameters. These can include, among other parameters, injection strength, bias current, and the intercavity distance between constituent elements. This analytical method can be universally applied regardless of the form of coupling at play albeit with some modifications according to the cavity geometries used. For the case of mutual injection, Han et al. numerically explore the dynamics of coupled nanolasers by considering the influence of the spontaneous emission factor β, the Purcell factor F, and the linewidth enhancement factor α for varying optical injection strengths and intercavity distances [39]. Tuning the injection strength alone, the authors can observe periodic oscillations and both stationary and nonstationary periodic doubling as illustrated in Figure 2A. More importantly, an enhanced stability of the coupled system with high values of F is reported, thus underlining the advantage of nanoscale lasers due to their pronounced Purcell factors [39].

Besides stable operation, the high-frequency periodic oscillations exhibited by a dual nanolaser system are also of interest for any applications requiring high speeds. Adams et al. [46] theoretically predict such periodic oscillations to occur outside the stability region for two laterally coupled nanowire lasers. The frequency of these oscillations as a function of both the separation between the nanolasers and the pumping rate is shown in Figure 2B. It can be clearly observed from the plot that ultrahigh frequencies on the order of at least 100 GHz can be reached when the separation is reduced to ~300 nm or so. Moreover, the oscillation frequency increases for larger pumping rates.

The studies used as examples in this subsection highlight the importance of investigating the dynamics of coupled nanolasers. Identifying the stable, oscillatory, and

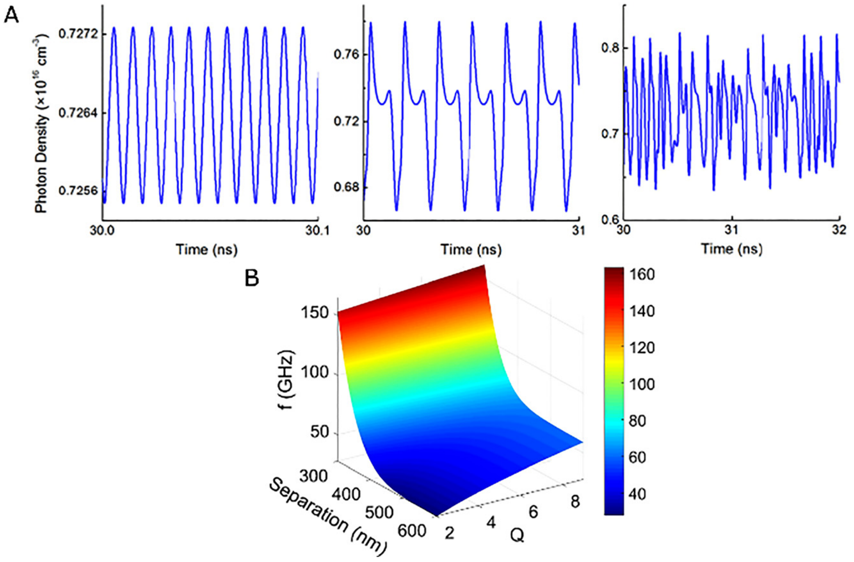

Figure 2: Periodic intensity oscillations. (A) Numerical simulations of photon density of one laser in a system of two mutually coupled nanolasers. Unstable dynamics such as periodic output (left), stationary period doubling (middle) or nonstationary period doubling (right) can be observed. Reprinted from a study by Han et al. [39] with permission. (B) Periodic oscillations for two evanescently coupled nanowires as a function of separation between lasers and pumping rate (*Q*). Oscillations can reach over 100 GHz. Reprinted from a study by Adams et al. [46] with permission.

chaotic regimes as a function of varying control parameters allows the coupled system to exhibit the desired behavior for the application demanded. Theoretical analyses can also shed light on bifurcations that can arise due to coupling. Such bifurcations are especially significant as they can lead to switching of optical modes as elaborated on in the next section.

2.3 Mode selection and switching

What is especially advantageous for nanoscale systems compared to their micron-sized counterparts, is their increased sensitivity to small perturbations induced by nuanced changes in the geometry or in the pumping scheme. These perturbations can result in alterations to the supermodes – such as the bonding and antibonding ones described in Section 2.1 – that are supported by the systems. Haddadi et al. [47] show in their study how varying the size of the middle row of holes in their coupled photonic crystal nanolaser structure can enable them to control the coupling behavior. In other words, by engineering the barrier between the two cavities (Figure 3A), both the amount of wavelength splitting as well as the excited state mode can be selected.

Figure 3B depicts the absolute value of the wavelength difference – $|\Delta\lambda|$ – between the bonding and antibonding supermodes as the barrier hole radius is varied. The distinct colors represent different radii of the nanocavities themselves. Through this graphic it can be inferred that the coupling strength can be tuned via the barrier size yielding either an increase or decrease in $|\Delta\lambda|$. Additionally, the authors report that the branches on either side of the dip in $|\Delta\lambda|$ correspond to a flip in the parity of the bonding mode. To be more accurate, to the left of the dip, the bonding mode becomes the excited state, whereas to the right, it remains the ground state mode [47]. Finally, increasing the size of the cavity results in a monotonic shift of the point where the parity flip of the bonding mode occurs. Efforts to select the ground state mode have also been reported in other studies, albeit with microcavities [48, 49].

Although static geometry tuning can determine the ground state supermode, alterations in the pumping scheme can lead to bifurcations which in turn, can allow for real-time switching between the coupled cavity modes. In their work, Marconi et al. [50] demonstrate that as they increase the optical pumping to their coupled photonic crystal nanolaser system, a mode-switching behavior is observed from the blue-detuned bonding mode to the red-detuned antibonding mode. Figure 3C portrays this switch for both simulated (top) and experimental (bottom) data. The mechanism behind the switching is attributed to the asymmetric stimulated light scattering induced by carrier oscillations which manifests itself through a Hopf bifurcation [50]. Such mode-beating oscillations and their corresponding decay rate were characterized through the statistical intensity experiments in the authors' more recent work [51].

Finally, in addition to switching between coupled supermodes that have dissimilar stability conditions, a spontaneous transition between coexisting eigenmodes is also possible, as demonstrated in quantum well-based photonic crystal nanolasers by Hamel et al. [36]. The light-out vs. light-in (*LL*) curve of the coupled system shown in Figure 3D illustrates that a pitchfork bifurcation occurs at a pump power $P = 1.33P_{th}$, where P_{th} is the lasing threshold. At this bifurcation point, the antibonding mode loses its

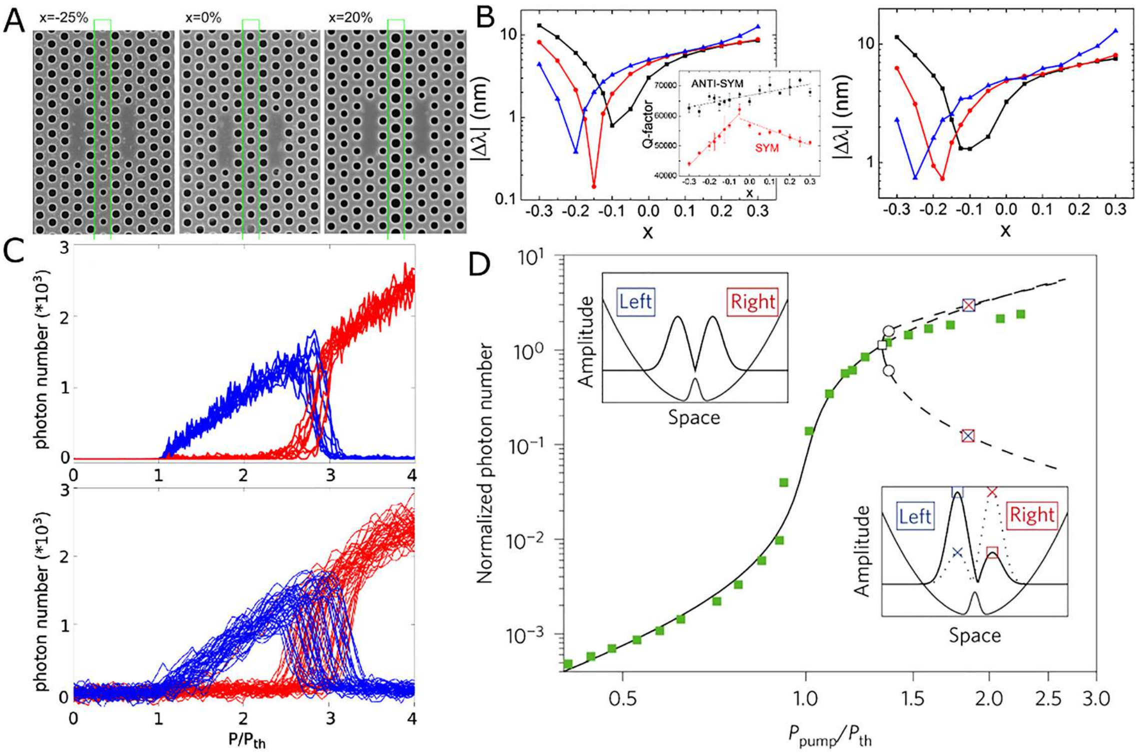

Figure 3: Mode selection and switching.
(A) Barrier engineering in photonic crystal nanolasers by changing size of the middle row of holes. For the case of $x = 0\%$, the radius of the highlighted row of holes is ~115 nm. (B) Absolute value of wavelength difference between B and AB modes – $|\Delta\lambda|$ – vs. size of the middle row of holes. Simulations (left) and experiment (right). Different colors represent different cavity sizes. The dip corresponds to the crossing or transition point where AB mode goes from being the excited state (right of dip) to becoming the ground state (left of dip); the opposite is true of the B mode. (A) and (B) adapted and reprinted from a study by Haddadi et al. [47] with permission. (C) Simulated (top) and experimental (bottom) results showing switching from B (blue) to AB (red) mode due to increased pump powers in two coupled photonic crystal nanolasers. Adapted from a study by Marconi et al. [50] with permission. (D) *LL* curve of two coupled photonic crystal nanolasers (green filled squares-experimental results; black solid line-numerical simulation) showing pitchfork bifurcation that results in two coexisting and stable, broken parity states (right inset). Left inset: Stable solution before bifurcation. Adapted from a study by Hamel et al. [36] with permission.

stability and two stable and coexisting solutions emerge. The first solution represents a high electric field amplitude in the left cavity and low amplitude in the right cavity [36]. The second solution is a mirror opposite of the first. For this spontaneous symmetry breaking to occur, the coupled nanolasers have to be designed with the exact parity and strength of the coupling coefficient needed to support these special states. The selective switching between the two stable states can then be triggered by pumping one of the cavities with a short pulse. Depending on the amplitude in the cavity prior to the incoming pulse, the state can either be retained or switched [36].

As evident from these results, the ability to engineer coupled modes as well as switch between them is of interest not only for the underlying physics involved but also for the potential applications. For instance, measuring the second order correlation function at zero delay – $g^2(0)$ – yields a value greater than 2 for a bonding supermode indicating the superthermal nature of light emitted from this mode [52]. For the antibonding mode, this value approaches 1 confirming lasing behavior. Therefore, systems where the mode selection is enabled are ideal test beds for important studies concerning quantum and nonlinear optics, out-of-equilibrium thermodynamics, quantum correlation devices, and engineering of superthermal sources [36, 50, 52]. Mode-switching devices with the ability to affect the transition between optical modes depending on the current state, as was explained for the broken parity states, can be said to exhibit memory and can therefore, be potentially used as ultracompact logic gates or optical flip flops [36].

2.4 Cross talk isolation

Although coupling between two nanolasers can yield complex dynamical phenomena rich in physics, certain applications might require the independent functioning of the emitters even when placed in close proximity. Biological sensing and imaging are two such areas, where maintaining isolation between the emission of the two cavities is imperative (discussed later in Section 3.1). This implies that each nanocavity can be pumped and modulated without influencing the behavior of its neighbor. For photonic crystal cavities mentioned previously, barrier engineering – where the barrier between the cavities is altered – is an effective method to inhibit the coupling [34, 46]. An alternative route taken to prevent coupling is to detune one cavity relative to the other via thermal or carrier effects [53].

In cavities that share a common cladding, such techniques are difficult to implement since any alterations made to one cavity will be transmitted to its neighbor via the shared cladding. For the case of metallo-dielectric nanolasers, the metallic coating serves as the common cladding for the two resonators. In such a scenario, a viable way to curb the evanescent interaction of the electromagnetic fields is to introduce a resonance mismatch by designing one cavity to be slightly larger than its neighbor. By doing so, Deka et al. [35] are able to demonstrate that the degree of splitting in the eigenmode frequency and optical loss – a characteristic signature of coupling – can be minimized. The case of equal-sized resonators was presented earlier (Figure 1C), where the pronounced splitting in the λ, Q, and g_{th} confirmed the effects of coupling. In order to mitigate this coupling, Deka et al. [35] altered the radius of one cavity to be 5% larger than its neighbor. This size mismatch yields splitting that is now hardly discernible, as depicted in Figure 4A, for the same parameters demonstrated in Figure 1C. This implies that despite the continual reduction in d as before, the dissimilar resonances now lead to inhibited coupling.

Another geometry-based technique that can be implemented to mitigate coupling in metallo-dielectric nanolasers is to increase the cavity radii in order to exploit the higher-order modes supported by larger cavities. Such modes exhibit stronger optical confinement to the gain media. As a result, less of the modes leaks out to evanescently interact with one another which is the exact phenomena that usually leads to the creation of coupled supermodes. This form of strong confinement of higher-order modes has been previously reported in microcavities [32, 54]. Pan et al. [55] demonstrate this behavior for the same dual metallo-dielectric nanolaser system first presented in a study by Deka et al. [35]. Figure 4B depicts their results, where the difference between the Q-factors – ΔQ – for the coupled mode for two different intercavity distances (d = 100 and 0 nm) are plotted as a function of the cavity radius. It can be clearly inferred from this plot that as the radii of the nanocavities are increased, the split in their losses diminishes due to reduced coupling.

Isolation between two emitters can also be ensured for forms of coupling besides just the evanescent interactions discussed above, such as for mutual injection coupling. In their numerical analysis, Han et al. consider the case of two mutually coupled but independently modulated nanolasers where, by tuning parameters such as the bias current, injection strength, and modulation depth, both unidirectional and bidirectional isolation can be achieved [56]. For instance, if one of the nanolasers is modulated at 50 GHz while the other at 20 GHz, for certain ranges of the bias current and injection strength, the dynamics of one laser is affected by the other but not vice versa. This result is encapsulated in Figure 4C, where the Fast Fourier Transforms (FFTs) of the photon densities of both lasers demonstrate unidirectional isolation. If the goal is to ensure bidirectional isolation, eliminating cross talk completely in the process, the bias current, injection strength, and modulation depth can be tuned accordingly [56]. Once this is achieved, Figure 4D shows that the same two lasers as before can be modulated independently with the dynamics of each unperturbed by the other. More importantly, the authors report that the zero cross talk regime can only be observed in coupled systems with large β and Purcell enhancement factors, which implies the suitability of nanolasers (which demonstrate intrinsic high-β and F) for use in PICs.

The studies reviewed in Section 2 emphasize the value of a two-nanolaser system as a test bed to further understanding of complex physics such as quantum and nonlinear optics, phase-locking, and cross talk isolation. For instance, when trying to implement independent control over each emitter, it is much easier to grasp the complex nonlinear dynamics involved by limiting the system size to just two. Next, we will discuss nanolaser arrays and how some of the ideas presented in this section can be scaled up and implemented in large-scale lattices.

3 Nanolaser arrays

Scaling up design to allow individual light sources to work in conjunction in an array format falls into the natural roadmap of the nanolaser technology [1, 2]. It is important to emphasize here, however, that not all nanolaser arrays rely on the same operating principles. The main distinction to be made is between uncoupled and coupled arrays. Uncoupled arrays comprise individual nanolasers that function independently and do not interact with their nearest neighbors. Some of the techniques to ensure isolation for two nanolaser systems reviewed in Section 2.4 can now be extended to ensure zero cross talk for dense

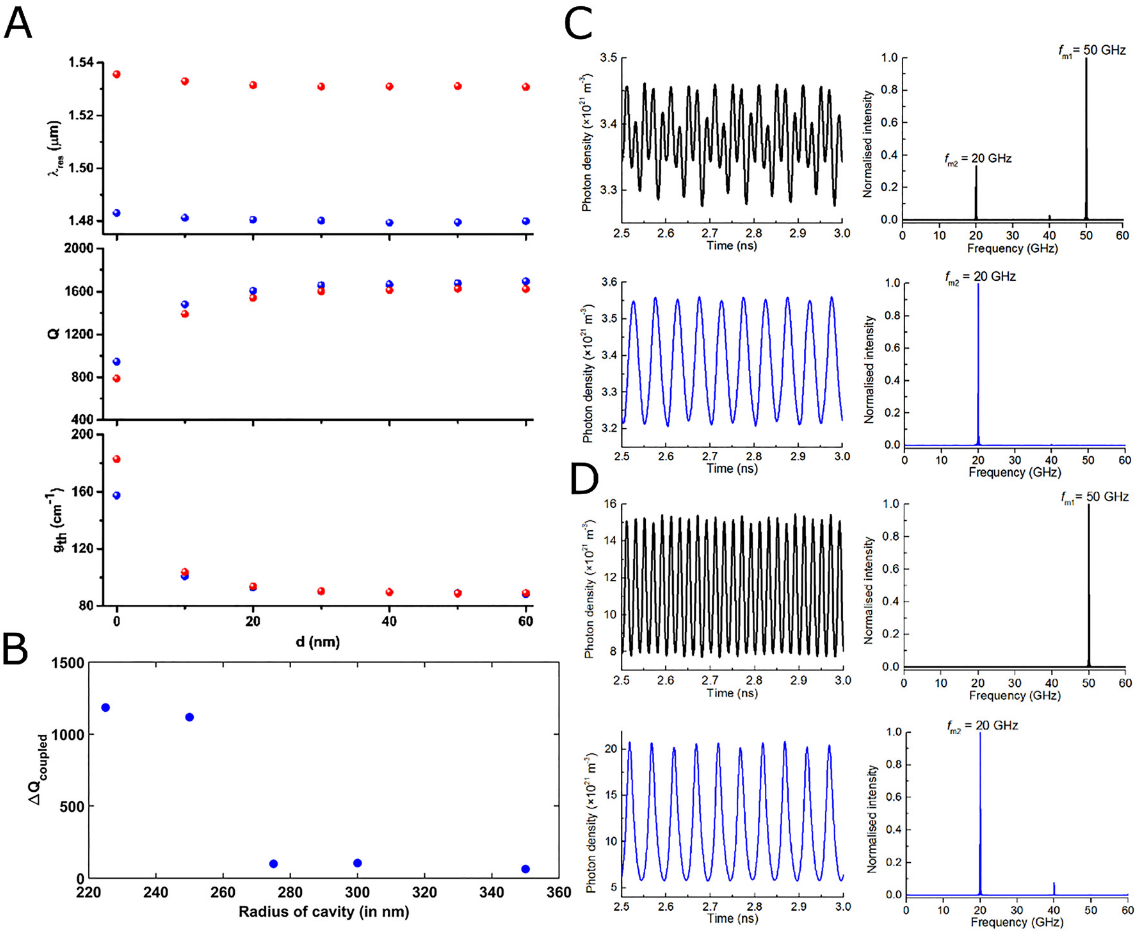

Figure 4: Cross talk isolation techniques.
(A) Eigenmode wavelengths (λ), quality factors (Q), and gain thresholds (g_{th}) for the two modes supported in two unequal sized metallo-dielectric cavities, where one is 5% larger in radius. Unlike in Figure 1C, no pronounced splitting is observed due to reduced coupling. Adapted from a study by Deka et al. [35] with permission. (B) Difference in Q for the coupled mode – ΔQcoupled – for $d = 100$ nm and $d = 0$ nm as a function of radii of the cavities. Larger sized cavities impede coupling. Reprinted from a study by Deka et al. [55] with permission. (C) Photon densities (left) and their Fast Fourier Transforms (FFTs, right) for two mutually coupled nanolasers in unidirectional isolation. Laser 1 (top) is affected by dynamics of laser 2 (bottom) but not vice versa. (D) Same as (C) but now nanolasers are in bidirectional isolation regime. Each laser is unperturbed by dynamics of its neighbor. (C) and (D) reprinted from a study by Han et al. [56] with permission.

lattices. In direct contrast, coupled arrays, as the name suggests, rely on coupling of some form involving the constituent resonators comprising the system. This may be exhibited either in terms of evanescent coupling between the nanocavities or excitonic state-plasmonic surface lattice resonance coupling. Owing to their clear disparity, coupled and uncoupled arrays are each appropriate for different types of applications.

3.1 Uncoupled arrays

Coupling, especially strong coupling, makes the task of distinguishing between the individual resonators more complex since the two (or multiple) emitters can now be viewed as a new, larger system [35]. Therefore, for applications that rely on the individual state or output of each element in the lattice, uncoupled arrays are most suitable. A majority of sensing and imaging applications fall into this category as they rely on recording the wavelength shift of each nanolaser due to changes in the refractive index environment.

One such study authored by Hachuda et al. [57] demonstrates the detection of protein in the form of streptavidin (SA) by using a 16-element 2D photonic crystal nanolaser array. The nanolaser geometry and array design, depicted in Figure 5A, show how a nanoslot is incorporated into the design. These nanoslots help with the localization of the optical mode which is especially significant, given that the measurements are performed in water to help with thermal stability [57, 58]. Although all the nanolasers are designed to be identical, the independence is maintained by optically pumping each one separately to record the red-shift in emission wavelength – $\Delta\lambda$ – caused by the adsorption of protein in each individual nanolaser. The overall wavelength alterations for all 16 devices are then statistically evaluated using averaging and confidence intervals.

Figure 5B portrays the results for $\Delta\lambda$ for each element in the array when impure solutions containing the protein SA are exposed to the nanolaser array. With water serving as the control (blue), it can be clearly observed that the array can distinguish between a sample containing SA (red) and those without it (black) based on the shift in emission wavelengths. In this experiment, bovine serum albumin (BSA) is treated as a contaminant to which the target protein, SA, is attached [57]. By averaging the results for all nanolasers in the array and increasing the amount of contaminant BSA, the limit of the array's sensitivity and selectivity can also be determined as shown in Figure 5C.

Based on the same principle of using $\Delta\lambda$ from individual lasers, Abe et al. [59] demonstrate imaging of living cells using uncoupled arrays comprising 21 × 21 = 441 photonic crystal nanolasers. In their study, the cross talk isolation between individual array constituents is ensured by designing an offset in radii for all neighboring lasers, an idea reviewed earlier in Section 2.4 [35]. Figure 6A illustrates that it is possible to optically pump the entire array yet maintain independent operation due to the radii mismatch engineered in the design. To perform imaging, the target cell was deposited on top of the nanolaser array, and the subsequent shift in the emission wavelength was recorded for each array element. The $\Delta\lambda$ image is created by measuring the reference λ for each nanolaser and then mapping the $\Delta\lambda$ at each laser's position in the array.

The results – illustrated in Figure 6B – not only provide an accurate albeit rough image of the cell but also demonstrate time evolution since the detection is continuous. Additionally, by employing nanoslots in their design, a Δn image is created which suppresses the noise and calibrates nonuniformity to yield a more accurate capture than its $\Delta\lambda$-based counterpart [59]. Figure 6C describes the ability of a Δn image to track the movement of a cell until it is desorbed, which in this case is shown to take upwards of 10 h.

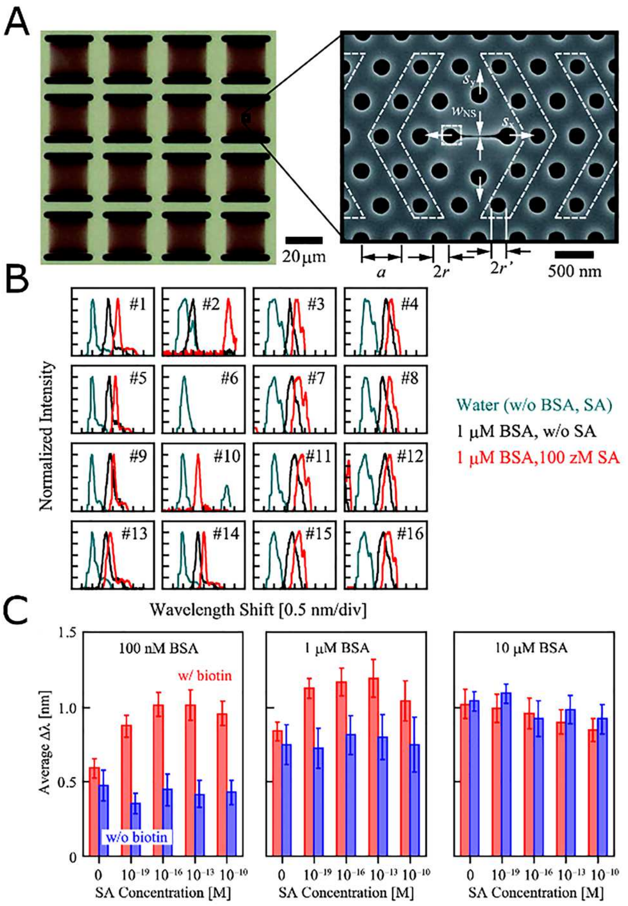

Figure 5: Biological sensing of proteins.
(A) Schematic of 16-element photonic crystal uncoupled array (left) and Scanning Electron Microscope (SEM) image of nanoslot-incorporated single laser (right). (B) Normalized intensity showing wavelength shift for all 16 elements under varying solutions. Water serves as the control. (C) Average wavelength shift calculated from all lasers – $\Delta\lambda$ – plotted for increasing amount of contaminant bovine serum albumin (BSA). Adapted and reprinted from a study by Hachuda et al. [57] with permission.

Besides sensing and imaging, uncoupled lasing arrays can also be purposed to address other complex problems. By creating organic molecule-based laser arrays and using them in conjunction with distinct organic solutions, Feng et al. [60] demonstrate the possibility of creating nondeterministic cryptographic primitives. The randomness in the size distribution of the individual nanolasers is caused by the stochastic manner in which the organic solution forms capillary bridges around the array elements. The varying array types formed with four distinct organic solutions is shown in Figure 7A. Owing to multiple vibrational sublevels, the organic molecule used in this study is capable of exhibiting dual wavelength lasing at either 660 or 720 nm or both depending on the length of the cavity. Figure 7B describes the emission behavior as a function of the cavity length for arrays created with the different solutions. Clearly, four distinct emission states can be observed depending on the stochastic size distribution of the nanolasers – (1) no lasing, (2) lasing at 660 nm only, (3) lasing at both 660 and 720 nm, and (4) lasing at 720 nm

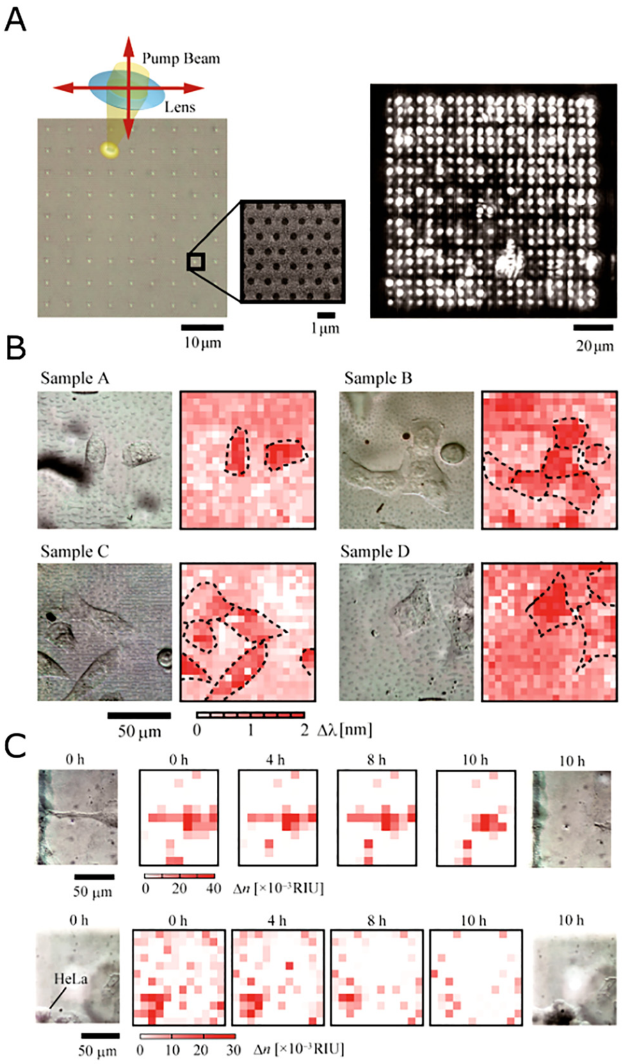

Figure 6: Imaging living cells.
(A) SEM image of uncoupled nanolaser array (left) and near-field emission of the array (right). (B) $\Delta\lambda$ image (right panels) of different samples of cells (optical micrographs; left panels) and (C) Δn image (center panels) tracking movement of a single cell (optical micrographs; left and right panels). Reprinted from a study by Abe et al. [59] with permission.

only. These states can be represented as either quaternary bits (‘0’ for no lasing, ‘1’ for lasing at 660 nm etc.) or double binary bits (‘00’ for no lasing, ‘01’ for lasing at 660 nm, etc.). In order to generate a cryptographic sequence from the arrays, each nanolaser is pumped separately with the pump then subsequently scanned to get the emission spectra from all other devices [60]. This technique, portrayed in Figure 7C, yields different encoding bits for each nanolaser (depending on its cavity length) which can be used to generate cryptographic bit sequences like in Figure 7D. In fact, encoding as double binary bits makes it possible to generate up to 2048 binary bits.

The studies elaborated above are only a fraction of the multiple works demonstrating how uncoupled arrays can achieve unique applications. Whether used for refractive index sensing, imaging or developing next generation, all-photonic cryptographic primitives, maintaining the independence of each nanolaser in the array is of vital importance for these applications [59–61]. Additionally, nanolaser arrays offer distinct advantages for some of these applications such as higher sensitivity compared to Raman-based sensors as well as a label-free imaging method [59, 61]. The use of such arrays can also be extended to telecommunications, lab-on-a-chip applications, spectroscopy, and parallel detection [62–64]. Finally, integration of up to 11,664 nanolasers has already been demonstrated in a photonic crystal uncoupled array, underlining the feasibility of achieving even higher on-chip packing density in the future [65].

3.2 Coupled arrays

Contrary to independent nanolaser operation in uncoupled arrays, coupling can give rise to different types of nonlinear dynamics and in general, increases the complexity of the physical mechanisms involved in the process. It is well worth investing effort to understand these underlying phenomena however, as coupling allows much greater control on the emission properties than is possible with uncoupled operation. Coupling in arrays has been demonstrated in a variety of manners including bound state in-continuum mode coupling [66, 67], interferential coupling [68], transverse-mode coupling [69], surface plasmon–based coupling [70–78], and evanescent coupling [40, 79–82]. We will focus this review mainly on the latter two forms since a majority of the literature on nanolaser arrays was found to rely primarily on these two mechanisms.

In order to present an idea of the breadth of functionalities enabled due to coupling, in this section, we review some of the relevant alterations to the emission along with the associated studies demonstrating the principle. It is important to note here that plasmon-based coupling is usually reported to affect properties of the emission such as directionality and wavelength. For most implementations of coupled arrays based on this physics, a lattice of metal nanoparticles creates the localized surface plasmon (LSP) resonance while some form of liquid dye medium, in which the lattice is immersed, serves as the gain or exciton states (ESs). This type of hybrid resonance is referred to as the ES-LSP. Although some aspects of the lasing phenomena are yet to be fully understood, the general consensus is that

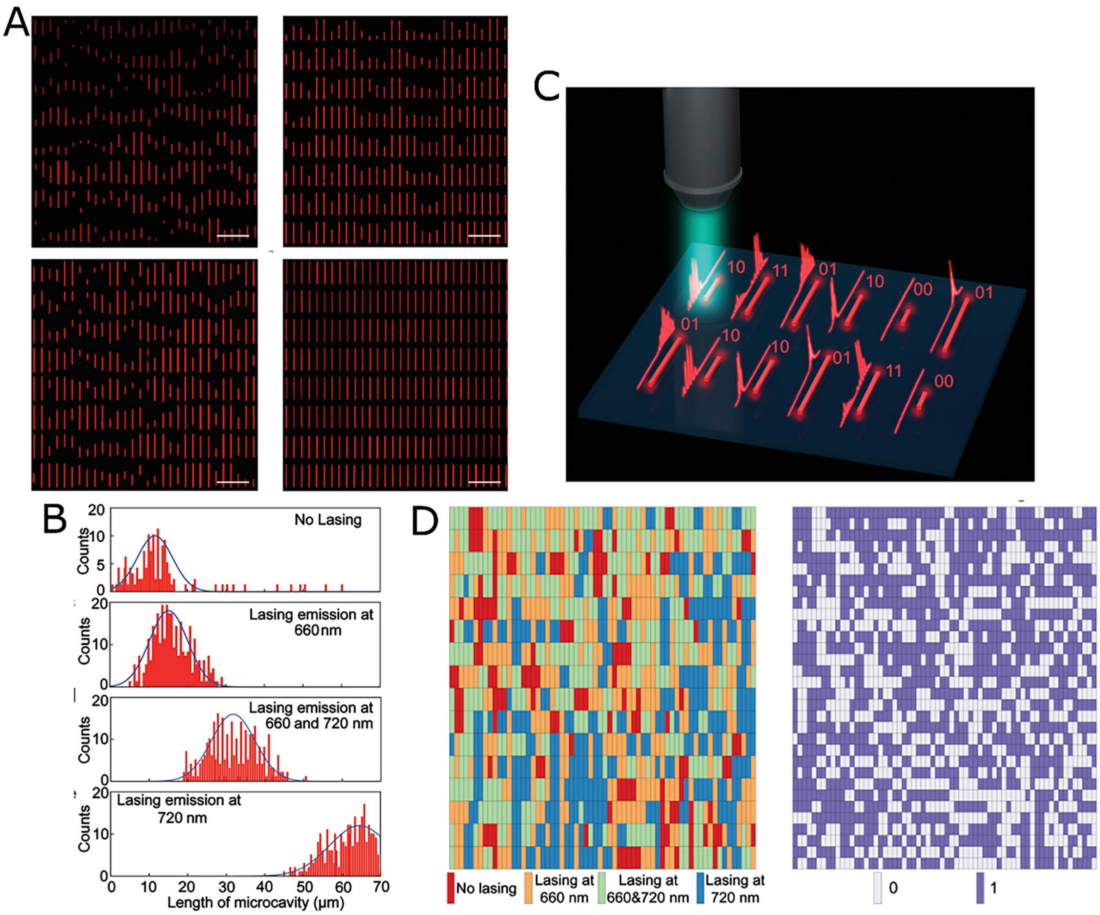

Figure 7: Optical cryptography.
(A) Organic nanolaser arrays with stochastic size distribution dependent on the organic solution used during fabrication. Scale bar: 100 μm. (B) Distribution of cavity lengths for four distinct emission states. The distribution illustrates how the length of the nanolaser determines the emission state. (C) Scanning of each individual nanolaser with a pump pulse. Depending on the emission state, the spectral information can be encoded as a bit. (D) Cryptographic sequence generated by treating emission states as quaternary bits (left) and double binary bits (right). Adapted and reprinted from a study by Feng et al. [60] with permission.

it occurs due to the excited-state molecules being stimulated to transfer energy to the lattice plasmons of the same frequency, phase, and polarization [72, 83]. In other words, the localized near-fields of the plasmonic particles comprising the array can stimulate the gain regions surrounding the particles to emit stimulated light at a wavelength that matches that of the lattice plasmon mode. With stimulated emission from the dye gain and a distributed cavity-like resonance provided by the lattice plasmon, lasing action can thus be obtained. It is important to note here that the reason for the tight confinement of light in these 2D metallic nanoparticle arrays is due to the strong interaction between the LSP resonances of individual particles and the far-field diffractive modes that satisfy the Bragg conditions of the array [84].

In comparison, evanescently coupled arrays can yield high powers and even generate states with orbital angular momentum (OAM) through the interplay between the lattice geometry and the modes of the individual lasers. Unlike for ES-LSP coupling where the resonance structure and gain are disparate media, for evanescent interactions, the active medium (usually comprised III-V semiconductors) is not external to the resonant structure; instead, it is a part of the cavity that supports the electromagnetic mode.

3.2.1 Beam directionality

Ability to control the direction of emission is of notable significance for wireless communications and nanoscale biosensors among other applications. A manner in which the angle of maximum emission from a nanolaser array can be modified involves altering the angle and/or polarization of the input optical pump. Zhou et al. [72] demonstrate this functionality by employing Au and Ag nanoparticle arrays immersed in a polymer gain comprising polyurethane and IR-140 dye gain. The schematic of the nanoparticle array is reproduced in Figure 8A, where the glass substrate and coverslip sandwich the lattice and gain layers. When the authors tune the pump angle to either be parallel to or 45° to the lattice direction, the far-field lasing beam patterns from the array are noticeably distinct as illustrated in Figure 8B. Depending on the angle of the pump, certain nanoparticles exhibit increased localizations of the electromagnetic mode, which in turn, affects the overall direction of the beam emitted from the array. It is also observed that the Ag array performed significantly better than its Au-based counterpart owing to reduced optical losses of the former [72].

Based on a similar though not identical material system as the work above, Meng et al. [73] also demonstrate highly directional lasing from their coupled spaser array. Their design consists of an Ag film with nanometer-sized holes, as opposed to nanoparticles, which is covered with an organic dye-polymer gain as shown in Figure 8C. Instead of altering the pump incidence angle, however, the detector itself is rotated to measure the directionality of the array output emission. Measuring the emission at varying detector angles along both the horizontal and vertical directions yields the results in Figure 8D. The narrow width of the measured emission as a function of the detector angle confirms the coherent, directional nature of the output beam. Lasing from this array is attributed to a surface plasmon polariton Bloch wave which also relies on some amount of feedback from plasmonic mode coupling between the Ag holes. The presence of the feedback is confirmed by the absence of lasing when an aperiodic lattice is used instead of a periodic one [71].

3.2.2 Tunable emission wavelength

Control over the emission wavelength of nanoscale light sources is desirable for dense wavelength division multiplexing (WDM) applications at a chip-scale level [85]. Other potential uses of tuning can be in lidar and imaging/sensing systems. In addition to achieving directionality of beam emission, it is also possible to alter the wavelength of output light from coupled arrays. Incidence angle and polarization of the pump can play a determining role in this respect as well. In one study, Knudson et al. [74] create a rhombohedral Al nanoparticle array which is then immersed in dye gain like the works referenced to in the previous section. Depending on the in-plane pump polarization, the ES-LSP–based mechanism leads to the array emitting at either 513 and 570 nm or both. This tuning of the output light from the array is described via Figure 9A and B which show the experimental streak camera images and numerically simulated spectra of the structure used in the study, respectively. The authors also elaborate on how

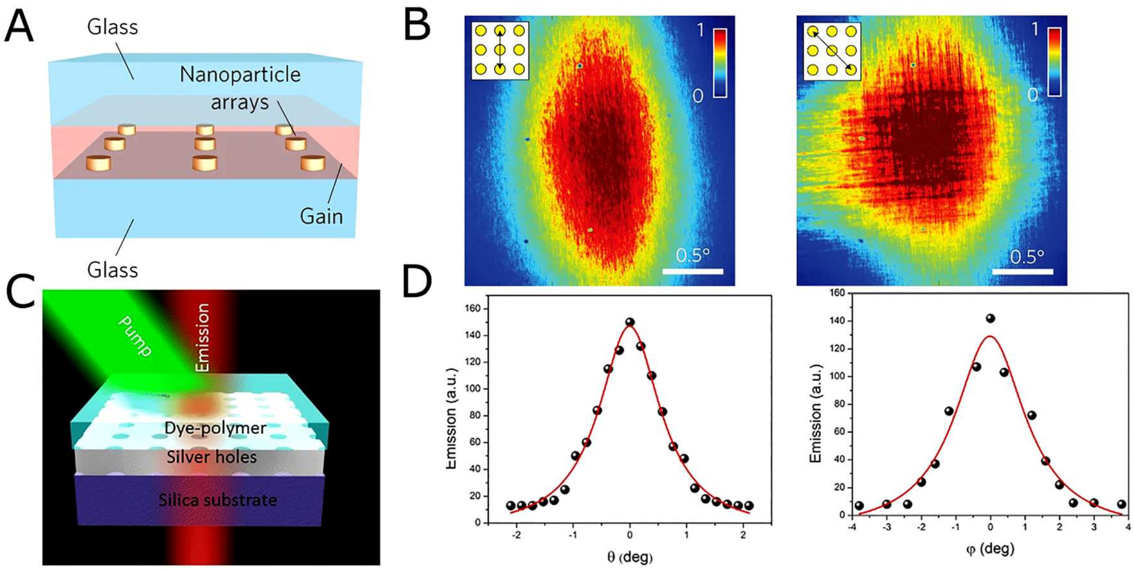

Figure 8: Directional emission.
(A) Schematic of metal nanoparticles embedded in dye gain and sandwiched between two glass slides. (B) Far-field emission patterns of the nanolaser array in (A) for pump incidence angle parallel to (left) and 45° (right) to the lattice direction. (A) and (B) adapted and reprinted from a study by Zhou et al. [72] with permission. (C) Schematic of Ag film with nanoholes immersed in dye-polymer gain. (D) Emission intensity from the coupled nanolaser array in (C) as the detector angle is varied along the horizontal (left) and vertical (right) directions. (C) and (D) adapted and reprinted from a study by Meng et al. [73] with permission.

selection of the nanoparticle shape comprising the array can determine the location of the electric field enhancement (i.e., the plasmon hotspots) [74]. In fact, other studies have demonstrated that unique shapes such as bowties can also exhibit ES-LSP–based nanocavity array lasing along with wavelength tuning [75]. Moreover, the Purcell factor is significantly enhanced due to the bowtie design, which in turn drives down the threshold allowing for room temperature lasing [75]. Finally, van Beijnum et al. [76] use a related phenomenon – surface plasmon associated lasing – to report that depending on the angle at which the emission from their array (comprising Au holes and InGaAs gain) is measured, the wavelength recorded varies.

Besides angle-resolved experiments to select the peak emission wavelength, altering the temperature is another technique that can be leveraged to attain the same goal. This may be accomplished via two main mechanisms: the first involves modifying the stoichiometry of the gain material based on thermal annealing. The second pertains to the temperature-induced red-shift of the bandgap commonly referred to as the Varshni shift [86]. Huang et al. [77] demonstrate a wavelength-tunable device based on the former principle by combining an Au/SiO_2 grating resonance with lead halide perovskite gain material. By thermally annealing their structure in a CH_3NH_3Br environment, the hybrid plasmonic mode in which the coupled nanolaser array operates in is observed to be blue-shifted in emission wavelength as shown in Figure 9C. More importantly, this modification of the wavelength is a reversible change and the original peak wavelength can be recovered after the annealing process [77].

Similar to thermal annealing-based alterations, tuning predicated on the Varshni shift is also caused by temperature acting as the catalyzing factor. However, the latter method differs in that it does not require any specific chemical environment to be implemented and the alteration in the emission wavelength is always a red-shift irrespective of the material. The pseudowedge plasmonic nanolaser array presented by Chou et al. [78] exhibits such a red-shift in the emission wavelength based on operating temperature. Their structure, consisting of a ZnO nanowire placed on an Ag grating (Figure 9D), forms an

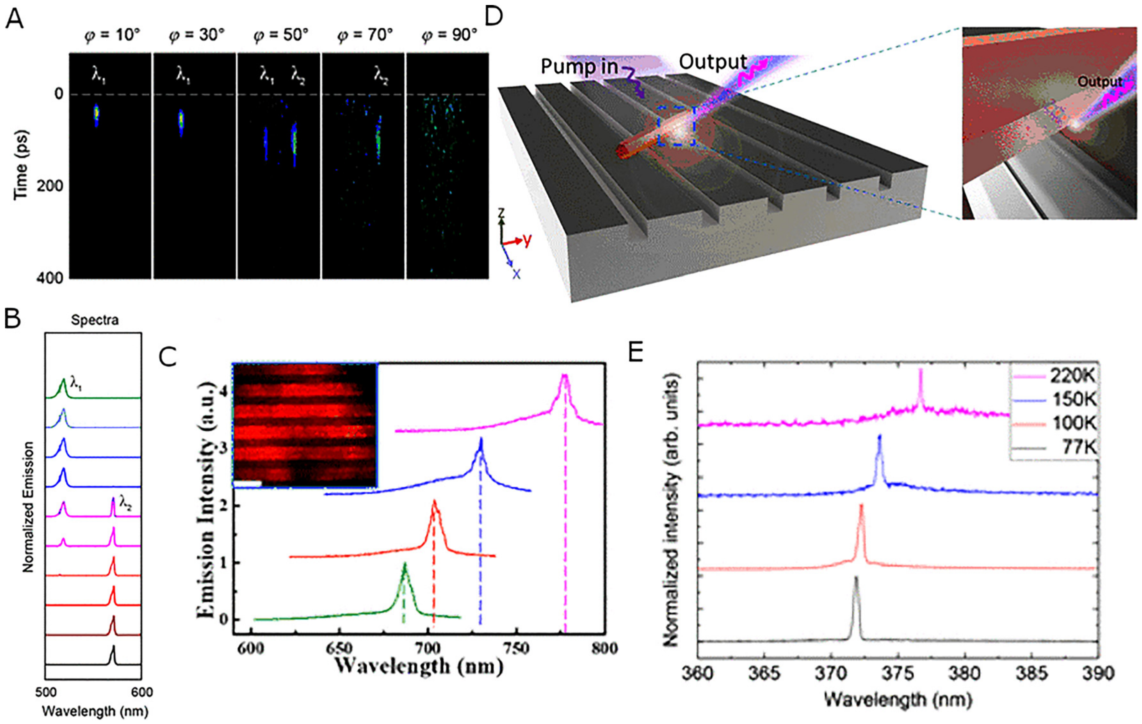

Figure 9: Tuning peak wavelength of emission.
(A) Experimental streak camera images of nanolaser array as the in-plane pump polarization is altered. (B) Numerical simulation of the spectra for varying pump polarization. (A) and (B) Adapted and reprinted from a study by Knudson et al. [74] with permission. (C) Spectra of nanolaser array as sample is annealed. A blue-shift in the peak wavelength occurs; Inset: Fluorescent microscope image of nanolaser array. Reprinted from a study by Huang et al. [77] with permission. (D) Schematic of pseudowedge nanolaser array with ZnO nanowire placed on top of Ag grating. (E) Varshni red-shift of emission wavelength as ambient temperature is increased. (D) and (E) adapted and reprinted from a study by Chou et al. [78].

unconventional array from the intersection points of the nanowire and the grating notches. This array displays single-mode lasing albeit subject to the manner in which the nanowire is positioned. By increasing the operating temperature from 77 to 220 K, the array undergoes a clear spectral red-shift as evidenced in Figure 9E due to the bandgap alterations in the ZnO caused by increased temperature.

3.2.3 Single and multimode switching

The studies on coupled arrays mentioned thus far portray instances of single-mode lasing. However, some specific cases such as multimode fiber–based WDM sources and on-chip multiplexing in photonic devices may also benefit from multimodal operation instead [87]. To meet the need in these niche areas, some studies such as the one authored by Wang et al. [70] have created ES-LSP nanolasing arrays with the capability to switch between the more common single-mode operation and a multimodal one. The researchers are able to do so by designing two distinct types of lattices – a single lattice where the individual nanoparticles collectively contribute to the resonance and a superlattice, where several single lattices combine to give rise to multiple band edge states. This contrast is displayed in Figure 10A, where the lasing emission from a single lattice (left, bottom) is seen to be single mode (right, bottom) while that from the superlattice (left, top) is observed to be multimodal in nature (right, top).

While single-mode and multimode operation can be demonstrated on individual lattices, an altered superlattice as illustrated in Figure 10B is designed to combine the two functionalities. This new design can be viewed as a single lattice from one direction and a superlattice from another. By doing so, both single and multimode emission are achieved from the same sample based on the polarization and direction of the input pump (Figure 10B). Specifically, if the pump direction is perpendicular to the lattice, the array operates in the single-mode lasing regime, whereas when the pump is parallel to the lattice direction, multimodal lasing is observed. In addition, the wavelength of emission can be tuned by altering either the size of the Au nanoparticles or the concentration of the dye gain comprising the nanostructure [70].

By choosing materials with unique properties for the coupled array, the applications for these devices can be extended to an even wider range of platforms. For instance, by employing a FM material like Ni to create nanodisk arrays in conjunction with dye gain, Pourjamal et al. [71] demonstrate the possibility of overcoming inherent losses in magnetoplasmonic systems. Their experimental results portrayed in Figure 10C underline the array's capability to switch between single and multimode lasing by modifying the particle periodicities in both the x and y directions. The authors claim that these arrays can potentially be used in the emerging field of topological photonics [71].

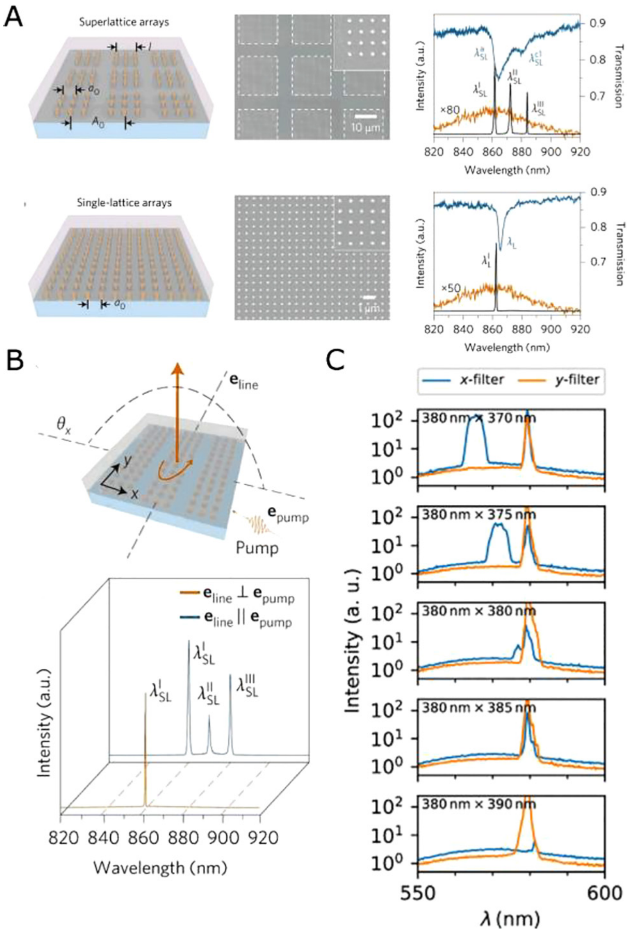

Figure 10: Switching between single and multimodal operation. (A) Schematic of superlattice and single lattice arrays (left), their SEM images (middle), and their corresponding spectra (right). The superlattice exhibits multimodal lasing (top, right), whereas the single lattice demonstrates single mode lasing (bottom, left) as evidenced by the lasing spectra shown as black solid curves in both figures. (B) Schematic of altered superlattice (top) and its output lasing spectra (bottom). If the pump direction is perpendicular to the lattice, the array operates in single mode lasing regime, whereas when the pump is parallel to the lattice direction, multimodal lasing is observed. (A) and (B) adapted and reprinted from a study by Wang et al. [70] with permission. (C) Experimental emission spectra for Ni nanodisk array for varying lattice periodicities. The presence of both x and y polarized modes confirms multimode lasing for some periodicities. Adapted and reprinted from a study by Pourjamal et al. [71] with permission.

3.2.4 Higher output power

Owing to their compact size, nanolasers inherently possess low power consumption characteristics and low output power [3]. However, if the lasers are designed and placed in close proximity such that the emission of a multitude of such lasers is coherently combined, a significantly higher output power can be obtained. The studies demonstrating this concept that are discussed in this section underline the great potential for nanolaser arrays to be employed in far-field applications, such as optical interconnects [2] and beam synthesis [88].

In their study based on a $N = 81$ element evanescently coupled photonic crystal nanolaser array, shown in Figure 11A, Altug et al. [79] are able to observe higher output powers with their coupled array than with a single emitter. Specifically, the maximum power achieved by the coupled array is found to be about ~100 times higher than that reached by the single cavity. More importantly, the coupled nanolaser array demonstrates a ~20-fold increase in the differential quantum efficiency (DQE) compared to their single laser counterpart. The DQE here refers to the slope of the *LL* curve above threshold and is extracted from the experimental results depicted in Figure 11B. Additionally, numerical analysis of the coupled rate equations reveals that with increasing *N*, both DQE and the maximum output power achievable show a corresponding increase (Figure 11C).

Increased output power has also been observed with other material systems such as metal-clad nanolaser arrays as reported by Hayenga et al. [80]. In this investigation, the overall power emitted by a seven-element metallic nanodisk array arranged in a hexagonal pattern (Figure 11D) is measured. The electromagnetic mode pattern supported by this design is first simulated and is shown in Figure 11D. Then, upon measurement, the output intensity of this array is found to be 35 times higher than that of a single nanodisk. Additionally, the array's slope efficiency is five times that of the single nanolaser. These results, encapsulated in Figure 11E, emphasize the ability to coherently combine the emission of multiple nanolasers to yield higher powers.

3.2.5 Orbital angular momentum

In addition to obtaining higher power, nanolasers may also be engineered to produce unique properties such as vortex beams with OAM in the far-field. Operating in such a state requires careful consideration of the lattice size, shape, and even type of nanolaser comprising the array. Hayenga

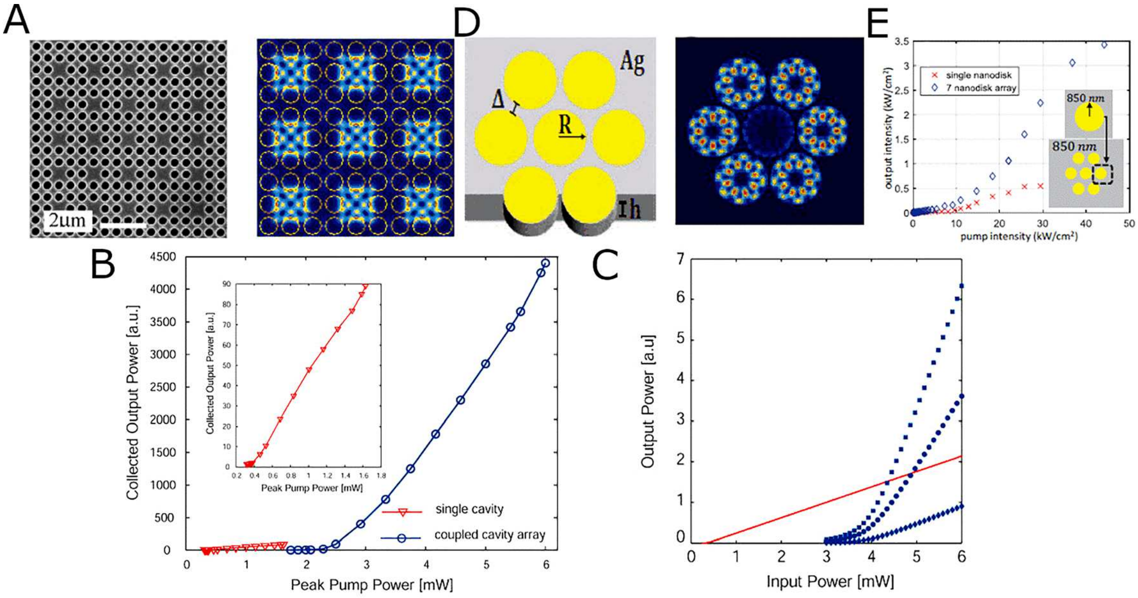

Figure 11: Higher output power.
(A) SEM image of photonic crystal nanolaser array (left) and simulation of the modes supported by the system (right). (B) Output power of coupled cavity array shown in (A) compared to that of a single cavity. Inset: Magnified version of curve for single cavity. (C) Numerical simulations of coupled rate equations comparing output power for single cavity (red) vs. that for a coupled cavity array with $N = 10$ (diamond), $N = 40$ (circle), and $N = 70$ (square). (A), (B), and (C) adapted and reprinted from a study by Altug[79] with permission. (D) Schematic of seven hexagonally designed metal-coated nanodisk lasers (left) and simulation of the mode structure supported (right). (E) Output intensity of one nanodisk vs. array as pump intensity is increased. Slope efficiency and power of array are much greater than that of single emitter. (D) and (E) adapted and reprinted from a study by Hayenga et al. [80] with permission.

et al. [81] demonstrate that by altering the types of evanescently coupled metallic nanolasers, it is possible to segment arrays into those that exclusively output vortex beams but do not carry OAM and those that display both characteristics. Specifically, an array of 500 nm diameter coaxial nanolasers exhibits the former, regardless of the array size, while a nanodisk array with 850 nm radius produces the latter as portrayed in Figure 12A and B, respectively. The dissimilarity in the two designs is explained by the interplay between the geometrical shape of the lattice and the whispering gallery modes supported by individual nanolasers. Whereas rotation is essential for higher order modes supported by the nanodisks to reduce the overlap with the lossy metal, it has no significant effect on the TE_{01} modes supported by the comparatively smaller-sized coaxial nanolasers. Furthermore, the topological charge associated with the beams carrying OAM can be tuned according to the number of lasers in the array as depicted in Figure 12C.

It is also possible to multiplex OAM beams with high topological charges using integrated microscale lasers as demonstrated by Bahari et al. [89] in a recent study. This is accomplished by designing circular boundaries between topologically distinct photonic crystal structures as shown in Figure 13A. In this Scanning Electron Microscope (SEM) image, rings 1 and 3 are composed of a photonic crystal with a nontrivial bandgap obtained by bonding InGaAsP multiple quantum wells on yttrium iron garnet (YIG). In contrast, ring 2 comprises a trivial bandgap photonic crystal. The dissimilarities in these concentric resonators gives rise to orthogonal OAM beams of alternating chirality [89]. In other words, the sign of the topological charge alternates as one moves from the innermost to the outermost ring. The chirality of the beams can also be reversed by applying an external magnetic field. Figure 13B demonstrates the far-field intensity patterns of OAM beams arising from each individual laser and also from the multiplexed array. The topological charges associated with rings 1, 2, and 3 are $|l_1| = 100$, $|l_2| = 156$, and $|l_3| = 276$, respectively. The observation of interference fringes in both theory and experiment for ring 2 is characteristic of beams carrying OAM. Although there is no coupling between the individual lasers in this array, it nevertheless presents a tantalizing possibility of dense integration of any arbitrary number of lasers for multiplexed OAM generation [89]. Generating such beams on a more compact platform based on nanolaser arrays can be a promising direction for future research.

Finally, another manner in which the properties of the beam emission such as OAM and directionality can be controlled is by choosing whether the topological nanolasers operate in a bulk or edge state. Using semiconductor nanodisk arrays, Shao et al. [90] demonstrate single-mode lasing from a bulk state by relying on band-inversion–

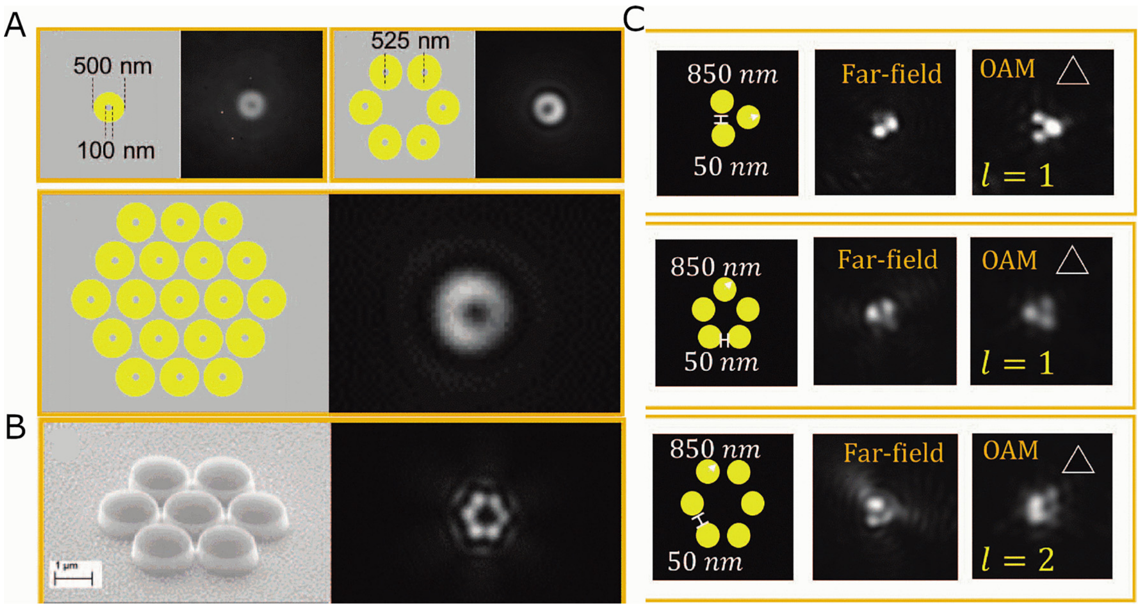

Figure 12: Vortex beams and orbital angular momentum.
(A) Schematics and experimental far-field mode structure for coaxial metal nanolasers of different array sizes. Vortex beam with no angular momentum is observed regardless of array size. (B) SEM image (left) and far-field mode structure of seven nanodisk array (right). A vortex beam with angular momentum is confirmed. (C) Varying nanodisk array sizes (left), their corresponding far-field patterns (middle), and their respective topological charges (right). (A), (B), and (C) adapted and reprinted from a study by Hayenga et al. [81] with permission.

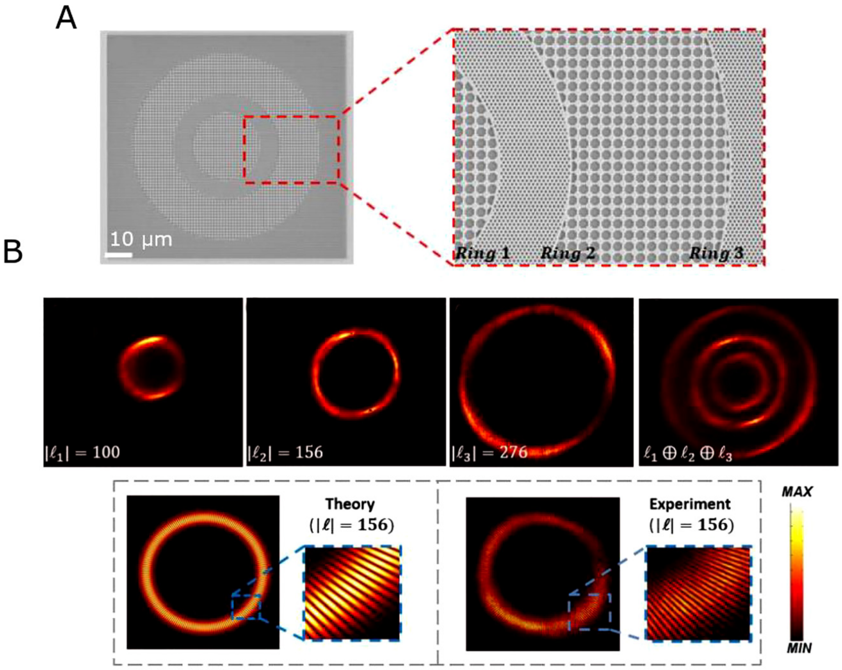

Figure 13: Multiplexed orbital angular momentum (OAM) beams.
(A) SEM image of three concentric ring lasers composed of two different photonic crystal structures. Inset: rings 1 and 3 are composed of a photonic crystal with a nontrivial bandgap obtained by bonding InGaAsP multiple quantum wells on yttrium iron garnet (YIG). In contrast, ring 2 comprises a trivial bandgap photonic crystal and cylindrical air-holes. (B) Measured far-field intensity of the rings showing their individual OAM beams (top row, first three images from left) and the multiplexed OAM beam formed (top row, far right image) when all rings are pumped simultaneously. The interference pattern observed in the far-field emission from ring 2 matches well with theory and confirms the OAM carried in the beams. (A) and (B) adapted and reprinted from a study by Bahari et al. [89] with permission.

induced reflection between trivial and topological photonic crystal cavities which exhibit opposite parities. As a result, although this bulk state mode does not carry OAM ($l = 0$), the emission is highly directional in the axis vertical to the cavity plane with divergence angles less than 6° and side-mode suppression ratios of over 36 dB. Based on a similar material system but with a slightly altered cavity design, authors from the same group are also able to observe lasing of spin-momentum–locked edge states [91]. In addition to vertical emission, the output beam from these cavities is observed to carry a topological charge of $l = -2$, while also allowing for higher side-mode suppression ratios of over 42 dB.

Creation of vectorial vortex beams such as the ones mentioned in the above studies can be of great value in areas such as imaging, optical trapping, and laser machining [92]. At the same time, beams carrying OAM can find applications in micromanipulation and both classical and quantum communication systems [93]. Therefore, the ability of nanolaser arrays to demonstrate useful attributes such as in-phase and out-of-phase supermodes and vortex beams with and without OAM makes them an ideal device platform for catering to a plethora of applications [40, 82].

4 Conclusion and future outlook

To conclude, recent progress on the development of array architectures of nanolasers is reviewed in this article. The focus was on valuable attributes realized due to unique array designs and the underlying physics that may help enable real-world applications such as biological sensing, imaging, and on-chip communications. A distinction was made between an array size of just two nanolasers and larger arrays. The former can not only serve as a testbed to understand the fundamental physics and enable interesting applications (for example optical flip flops) but also as a building block that can aid in comprehension of larger-lattice behavior. Larger arrays themselves can also be distinguished depending on whether their constituent elements function independently from one another or demonstrate coupling of some form. Uncoupled arrays are more intuitive to understand and suitable for applications such as imaging, biosensing, and even cryptography. On the other hand, although coupling in nanolaser arrays can create complex dynamics, control over many aspects of the emission behavior such as beam directionality, mode switching, and OAM are afforded.

In fact, it is in the area of coupled arrays that further research efforts are required owing to some important applications that still need to be experimentally demonstrated.

4.1 Phase-locked laser arrays

As mentioned previously in Section 2, the coupling between nanolasers can yield a plethora of dynamical regimes such as periodic intensity oscillations, chaotic fluctuations, and stable phase-locking. Among these, the regime of stable phase-locking holds great potential as it can help in the realization of phase-locked laser arrays with demonstrably higher power. Though the ability of evanescently coupled nanolasers to generate higher power has already been experimentally demonstrated, the studies mainly focused on how the accumulated power and slope efficiency of the arrays exceeded those of single emitters [79, 80]. Ideally, if all the constituent lasers are locked in-phase, their electric field amplitudes will interfere constructively, and the resulting far-field power density can be much greater than without in-phase locking. Specifically, for an array of N identical nanolasers with identical output intensities, the far-field power density that is measured will be N^2 times greater than that of a single nanolaser. Note here that the greater power density that is afforded is simply due to the coherent superposition of field amplitudes of the emitted waves, which means that conservation of energy is not violated in any manner.

Achieving in-phase stable locking, however, is not trivial as the stability regions are narrow and sensitive to the parameters in the rate equations, especially so for semiconductor lasers [42]. In a past work, Shahin et al. [94] demonstrated this increased sensitivity to the tuning parameters by considering the case of three free-running semiconductor lasers coupled to each other via optoelectronic feedback. The researchers observed that distinct dynamical regimes of operation can be achieved with their system including winner-takes-all (WTA), winner-shares-all (WSA), and winnerless competitions [94]. To gauge the stability of these different regimes, the coupled rate equations from a study by Shahin et al. [94] are numerically solved for the steady-state behaviors while varying the feedback coupling strength (ξ_{32}) as well as the detuning (Ω_{12}) between two of the lasers. This allows us to create a bifurcation map (shown in Figure 14A) for the same system considered in a study by Shahin et al. [94]. In this diagram, the different dynamical regimes are represented by color codes such as black for chaos, red for WTA competition, yellow for WSA competition, and white for winnerless competition. It is evident from the diagram, that the network of three coupled semiconductor lasers has numerous small regions of stability and for the slightest variation in the input parameters, the system transitions from one state to the other. This makes the system extremely unstable, thus rendering it challenging to put it to practical use.

Nanolasers inherently possess certain attributes such as high-β's and Purcell factors that can help alleviate this issue of instability as theorized in some works [42, 43, 95]. To demonstrate the effects such parameters can have on

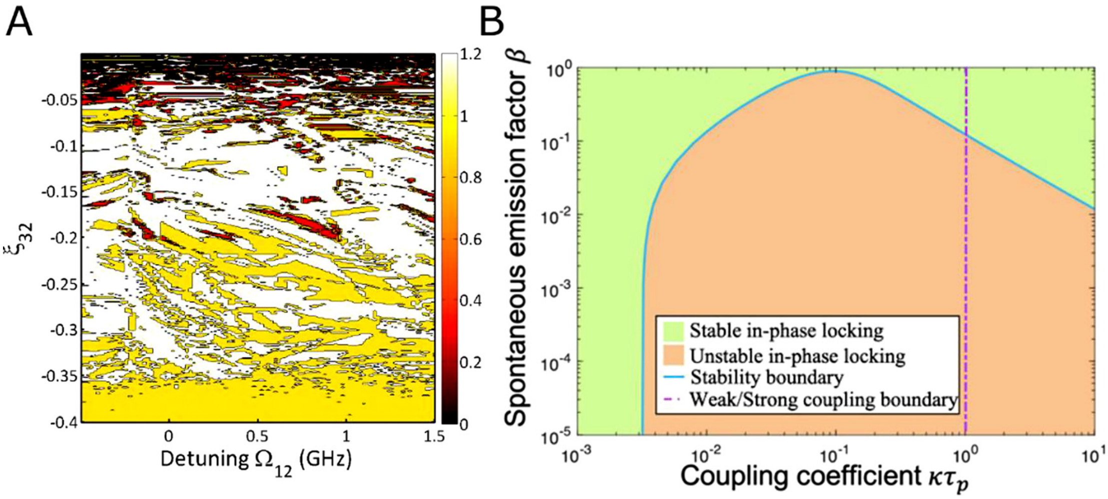

Figure 14: Stability maps.
(A) Calculated bifurcation diagram of three optoelectronically coupled free running semiconductor lasers as a function of detuning Ω_{12} and the coupling coefficient ξ_{32}. Varying system dynamics are observed such as chaos (magnitude of 0 in the color bar with black color), winner-takes-all (WTA) competition (magnitude of 0.5 with red color), winner-shares-all (WSA) competition (magnitude of 1 with yellow color), and winnerless competition (magnitude of 1.2 with white color). (B) Stability regions for two laterally coupled metallo-dielectric nanolasers as a function of coupling coefficient κ and spontaneous emission factor β. The dash-dotted purple line demarcates the weak coupling ($\kappa\tau_p < 1$) and strong coupling ($\kappa\tau_p > 1$) regions.

the stability, the coupled laser rate equations for two laterally coupled metallo-dielectric nanolasers are numerically solved. These equations are shown below:

$$\begin{aligned}\frac{dE_{1,2}}{dt} &= \frac{1}{2}(1+i\alpha)\left(\Gamma G(N_{1,2}) - \frac{1}{\tau_p}\right)E_{1,2} + iw_{1,2}E_{1,2} \\ &\&doublehyphen; 29pt + \frac{\Gamma F_p \beta N_{1,2}}{2\tau_{\mathrm{rad}}\left|E_{1,2}\right|^2}E_{1,2} + i\kappa E_{2,1}\,,\end{aligned} \tag{1}$$

$$\begin{aligned}\frac{dN_{1,2}}{dt} &= P - \frac{N_{1,2}}{\tau_{nr}} - \frac{(F_p\beta + 1 - \beta)N_{1,2}}{\tau_{\mathrm{rad}}} \\ &\&doublehyphen; 17pt - G(N_{1,2})\left|E_{1,2}\right|^2\,,\end{aligned} \tag{2}$$

where $E_{1,2}$ are the electric field amplitudes, $N_{1,2}$ are the carrier densities, $w_{1,2}$ are the intrinsic resonance frequencies, α is the phase-amplitude coupling (Henry) factor for a quantum well laser, $G(N)$ is the carrier density-dependent gain function, τ_p is photon lifetime, Γ is the confinement factor, F_p is Purcell enhancement factor, τ_{rad} and τ_{nr} are the radiative and nonradiative recombination lifetimes of the carriers, respectively, and P is the pump rate. The subscripts denote the two cavities that are coupled to each other.

By solving for the steady state solutions of equations (1) and (2), Figure 14B is created which illustrates how the stability region is affected by both β as well as the coupling coefficient κ. It can be inferred from the plot that although varying κ yields a more complex effect, higher values of β contribute to increased possibility of achieving in-phase locking. Therefore, what is now needed in this regard is further analysis and experimental demonstration of how parameters unique to nanolasers as well as other key parameters (such as frequency detuning, linewidth enhancement factor and pump rate) can enable easier in-phase locking.

Whereas near-field coupling can lead to higher powers via in-phase stable locking, far-field coupling can also be used to realize this goal. In addition, combining far-field coupling with control over the phase and amplitude of individual nanolasers in an array can result in an optical phased array with both frequency and phase tunability, akin to RF phased arrays. The methods to achieve directionality in array beam emission demonstrated thus far are limited to altering the incidence angle/polarization of the pump. In contrast, a true optical phased array of nanolasers can offer multiple degrees of freedom and much more nuanced control of the directionality since each emitter in the array can be individually tuned in both frequency and phase. Such far-field coupling with quantum cascade laser arrays has already been demonstrated [96]. The challenge that lies ahead is to achieve the same for subwavelength nanolaser arrays and preferably, with current injection.

4.2 Ultrashort pulse generation

When discussing nanolasers, an often-overlooked topic is ultrashort pulse generation. Typically, such pulses are created using mode-locking techniques, which can include both active and passive mode-locking. Due to the need for external design elements such as saturable absorbers or electro-optic modulators, achieving mode-locking with nanoscale lasers faces impediments. However, Gongora et al. [97] demonstrate in a recent work that it is in fact possible to mode-lock nanolasers in an array without external design elements by relying on the nonradiative nature of anapole states. Using this technique, the authors numerically demonstrate an ultrashort pulse down to 95 fs generated from an array whose constituent nanolasers are spaced apart evenly in frequency from one another to mirror mode-spacing in traditional mode-locking theory. It is also observed that the position of the nanolasers can alter the duration of the pulse generated [97]. Despite this result, experimental results of mode-locked nanolasers for ultrashort pulse generation are yet to be demonstrated. Doing so can unlock a wealth of applications in areas requiring short optical pulses such as LiDAR, optical regeneration, nonlinear optics, and optical sampling [98].

Author contribution: All the authors have accepted responsibility for the entire content of this submitted manuscript and approved submission.

Research funding: This work was supported by the Army Research Office (ARO), the Defense Advanced Research Projects Agency (DARPA) DSO NLM and NAC Programs, the Office of Naval Research (ONR), the National Science Foundation (NSF) grants DMR-1707641, CBET-1704085, NSF ECCS-180789, CCF-1640227, NSF ECCS-190184, the San Diego Nanotechnology Infrastructure (SDNI) supported by the NSF National Nanotechnology Coordinated Infrastructure (grant ECCS-1542148), Advanced Research Projects Agency—Energy (LEED: A Lightwave Energy-Efficient Datacenter), and the Cymer Corporation.

Conflict of interest statement: The authors declare no conflicts of interest.

References

[1] M. Smit, J. J. Van der Tol, and M. Hill, “Moore’s law in photonics,” *Laser Photonics Rev.*, vol. 6, pp. 1–3, 2012.

[2] R. M. Ma and R. F. Oulton, “Applications of nanolasers,” *Nat. Nanotechnol.*, vol. 14, pp. 12–22, 2019.

[3] M. T. Hill and M. C. Gather, “Advances in small lasers,” *Nat. Photonics*, vol. 8, p. 908, 2014.

[4] Q. Gu, J. S. Smalley, M. P. Nezhad, et al., “Subwavelength semiconductor lasers for dense chip-scale integration,” *Adv. Opt. Photonics*, vol. 6, pp. 1–56, 2014.
[5] H. Altug, D. Englund, and J. Vučković, “Ultrafast photonic crystal nanocavity laser,” *Nat. Phys.*, vol. 2, pp. 484–488, 2006.
[6] K. Nozaki, S. Kita, and T. Baba, “Room temperature continuous wave operation and controlled spontaneous emission in ultrasmall photonic crystal nanolaser,” *Opt. Express*, vol. 15, pp. 7506–7514, 2007.
[7] S. H. Kim, J. H. Choi, S. K. Lee, et al., “Optofluidic integration of a photonic crystal nanolaser,” *Opt. Express*, vol. 16, pp. 6515–6527, 2008.
[8] S. Matsuo, A. Shinya, T. Kakitsuka, et al., “High-speed ultracompact buried heterostructure photonic-crystal laser with 13 fJ of energy consumed per bit transmitted,” *Nat. Photonics*, vol. 4, p. 648, 2010.
[9] M. T. Hill, Y. S. Oei, B. Smalbrugge, et al., “Lasing in metallic-coated nanocavities,” *Nat. Photonics*, vol. 1, p. 589, 2007.
[10] M. P. Nezhad, A. Simic, O. Bondarenko, et al., “Room-temperature subwavelength metallo-dielectric lasers,” *Nat. Photonics*, vol. 4, p. 395, 2010.
[11] K. Ding, Z. C. Liu, L. J. Yin, et al., “Room-temperature continuous wave lasing in deep-subwavelength metallic cavities under electrical injection,” *Phys. Rev. B*, vol. 85, p. 041301, 2012.
[12] K. Ding, M. T. Hill, Z. C. Liu, L. J. Yin, P. J. Van Veldhoven, and C. Z. Ning, “Record performance of electrical injection sub-wavelength metallic-cavity semiconductor lasers at room temperature,” *Opt. Express*, vol. 21, pp. 4728–4733, 2013.
[13] Q. Gu, J. Shane, F. Vallini, et al., “Amorphous Al_2O_3 shield for thermal management in electrically pumped metallo-dielectric nanolasers,” *IEEE J. Quant. Electron.*, vol. 50, pp. 499–509, 2014.
[14] S. H. Pan, Q. Gu, A. El Amili, F. Vallini, and Y. Fainman, “Dynamic hysteresis in a coherent high-β nanolaser,” *Optica*, vol. 3, pp. 1260–1265, 2016.
[15] C. Y. Fang, S. H. Pan, F. Vallini, et al., “Lasing action in low-resistance nanolasers based on tunnel junctions,” *Opt. Lett.*, vol. 44, pp. 3669–3672, 2019.
[16] M. Khajavikhan, A. Simic, M. Katz, et al., “Thresholdless nanoscale coaxial lasers,” *Nature*, vol. 482, pp. 204–207, 2012.
[17] W. E. Hayenga, H. Garcia-Gracia, H. Hodaei, et al., “Second-order coherence properties of metallic nanolasers,” *Optica*, vol. 3, pp. 1187–1193, 2016.
[18] M. A. Noginov, G. Zhu, A. M. Belgrave, et al., “Demonstration of a spaser-based nanolaser,” *Nature*, vol. 460, pp. 1110–1112, 2009.
[19] R. F. Oulton, V. J. Sorger, T. Zentgraf, et al., “Plasmon lasers at deep subwavelength scale,” *Nature*, vol. 461, pp. 629–632, 2009.
[20] Y. J. Lu, J. Kim, H. Y. Chen, et al., “Plasmonic nanolaser using epitaxially grown silver film,” *Science*, vol. 337, pp. 450–453, 2012.
[21] Y. J. Lu, C. Y. Wang, J. Kim, et al., “All-color plasmonic nanolasers with ultralow thresholds: autotuning mechanism for single-mode lasing,” *Nano Lett.*, vol. 14, pp. 4381–4388, 2014.
[22] Y. H. Chou, Y. M. Wu, K. B. Hong, et al., “High-operation-temperature plasmonic nanolasers on single-crystalline aluminum,” *Nano Lett.*, vol. 16, pp. 3179–3186, 2016.
[23] M. I. Stockman, “Nanoplasmonic sensing and detection,” *Science*, vol. 348, pp. 287–288, 2015.
[24] E. I. Galanzha, R. Weingold, D. A. Nedosekin, et al., “Spaser as a biological probe,” *Nat. Commun.*, vol. 8, p. 15528, 2017.
[25] J. A. Schuller, E. S. Barnard, W. Cai, Y. C. Jun, J. S. White, and M. L. Brongersma, “Plasmonics for extreme light concentration and manipulation,” *Nat. Mater.*, vol. 9, pp. 193–204, 2010.
[26] S. Cho, M. Humar, N. Martino, and S. H. Yun, “Laser particle stimulated emission microscopy,” *Phys. Rev. Lett.*, vol. 117, p. 193902, 2016.
[27] D. A. Miller, “Device requirements for optical interconnects to silicon chips,” *Proc. IEEE*, vol. 97, pp. 1166–1185, 2009.
[28] C. Henry, “Theory of the linewidth of semiconductor lasers,” *IEEE J. Quant. Electron.*, vol. 18, pp. 259–264, 1982.
[29] A. Nakagawa, S. Ishii, and T. Baba, “Photonic molecule laser composed of GaInAsP microdisks,” *Appl. Phys. Lett.*, vol. 86, p. 041112, 2005.
[30] S. V. Boriskina, “Spectrally engineered photonic molecules as optical sensors with enhanced sensitivity: a proposal and numerical analysis,” *JOSA B*, vol. 23, pp. 1565–1573, 2006.
[31] S. V. Boriskina, “Coupling of whispering-gallery modes in size-mismatched microdisk photonic molecules,” *Opt. Lett.*, vol. 32, pp. 1557–1559, 2007.
[32] E. I. Smotrova, A. I. Nosich, T. M. Benson, and P. Sewell, “Optical coupling of whispering-gallery modes of two identical microdisks and its effect on photonic molecule lasing,” *IEEE J. Sel. Top. Quant. Electron.*, vol. 12, pp. 78–85, 2006.
[33] S. Ishii, A. Nakagawa, and T. Baba, “Modal characteristics and bistability in twin microdisk photonic molecule lasers,” *IEEE J. Sel. Top. Quant. Electron.*, vol. 12, pp. 71–77, 2006.
[34] K. A. Atlasov, K. F. Karlsson, A. Rudra, B. Dwir, and E. Kapon, “Wavelength and loss splitting in directly coupled photonic-crystal defect microcavities,” *Opt. Express*, vol. 16, pp. 16255–16264, 2008.
[35] S. S. Deka, S. H. Pan, Q. Gu, Y. Fainman, and A. El Amili, “Coupling in a dual metallo-dielectric nanolaser system,” *Opt. Lett.*, vol. 42, pp. 4760–4763, 2017.
[36] P. Hamel, S. Haddadi, F. Raineri, et al., “Spontaneous mirror-symmetry breaking in coupled photonic-crystal nanolasers,” *Nat. Photonics*, vol. 9, pp. 311–315, 2015.
[37] A. M. Yacomotti, S. Haddadi, and S. Barbay, “Self-pulsing nanocavity laser,” *Phys. Rev. A*, vol. 87, 2013, https://doi.org/10.1103/physreva.87.041804.
[38] M. J. Adams, N. Li, B. R. Cemlyn, H. Susanto, and I. D. Henning, “Effects of detuning, gain-guiding, and index antiguiding on the dynamics of two laterally coupled semiconductor lasers,” *Phys. Rev. A*, vol. 95, p. 053869, 2017.
[39] H. Han and K. A. Shore, “Dynamics and stability of mutually coupled nano-lasers,” *IEEE J. Quant. Electron.*, vol. 52, pp. 1–6, 2016.
[40] M. Parto, W. Hayenga, A. Marandi, D. N. Christodoulides, and M. Khajavikhan, “Realizing spin Hamiltonians in nanoscale active photonic lattices,” *Nat. Mater.*, vol. 19, pp. 725–731, 2020.
[41] M. Parto, W. E. Hayenga, A. Marandi, D. N. Christodoulides, and M. Khajavikhan, “Nanolaser-based emulators of spin Hamiltonians,” *Nanophotonics*, vol. 9, pp. 4193–4198, 2020.
[42] H. G. Winful and S. S. Wang, “Stability of phase locking in coupled semiconductor laser arrays,” *Appl. Phys. Lett.*, vol. 53, pp. 1894–1896, 1988.
[43] S. S. Wang and H. G. Winful, “Dynamics of phase-locked semiconductor laser arrays,” *Appl. Phys. Lett.*, vol. 52, pp. 1774–1776, 1988.

[44] S. Ji, Y. Hong, P. S. Spencer, J. Benedikt, and I. Davies, "Broad tunable photonic microwave generation based on period-one dynamics of optical injection vertical-cavity surface-emitting lasers," *Opt. Express*, vol. 25, pp. 19863–19871, 2017.

[45] X. Porte, M. C. Soriano, D. Brunner, and I. Fischer, "Bidirectional private key exchange using delay-coupled semiconductor lasers," *Opt. Lett.*, vol. 41, pp. 2871–2874, 2016.

[46] M. J. Adams, D. Jevtics, M. J. Strain, I. D. Henning, and A. Hurtado, "High-frequency dynamics of evanescently-coupled nanowire lasers," *Sci. Rep.*, vol. 9, pp. 1–7, 2019.

[47] S. Haddadi, P. Hamel, G. Beaudoin, et al., "Photonic molecules: tailoring the coupling strength and sign," *Opt. Express*, vol. 22, pp. 12359–12368, 2014.

[48] N. Caselli, F. Intonti, F. Riboli, et al., "Antibonding ground state in photonic crystal molecules," *Phys. Rev. B*, vol. 86, p. 035133, 2012.

[49] N. Caselli, F. Intonti, F. Riboli, and M. Gurioli, "Engineering the mode parity of the ground state in photonic crystal molecules," *Opt. Express*, vol. 22, pp. 4953–4959, 2014.

[50] M. Marconi, J. Javaloyes, F. Raineri, J. A. Levenson, and A. M. Yacomotti, "Asymmetric mode scattering in strongly coupled photonic crystal nanolasers," *Opt. Lett.*, vol. 41, pp. 5628–5631, 2016.

[51] M. Marconi, F. Raineri, A. Levenson, et al., "Mesoscopic limit cycles in coupled nanolasers," *Phys. Rev. Lett.*, vol. 124, p. 213602, 2020.

[52] M. Marconi, J. Javaloyes, P. Hamel, F. Raineri, A. Levenson, and A. M. Yacomotti, "Far-from-equilibrium route to superthermal light in bimodal nanolasers," *Phys. Rev. X*, vol. 8, p. 011013, 2018.

[53] D. O'Brien, M. D. Settle, T. Karle, A. Michaeli, M. Salib, and T. F. Krauss, "Coupled photonic crystal heterostructure nanocavities," *Opt. Express*, vol. 15, pp. 1228–1233, 2007.

[54] Q. Wang, H. Zhao, X. Du, W. Zhang, M. Qiu, and Q. Li, "Hybrid photonic-plasmonic molecule based on metal/Si disks," *Opt. Express*, vol. 21, pp. 11037–11047, 2013.

[55] S. H. Pan, S. S. Deka, A. El Amili, Q. Gu, and Y. Fainman, "Nanolasers: second-order intensity correlation, direct modulation and electromagnetic isolation in array architectures," *Prog. Quant. Electron.*, vol. 59, pp. 1–8, 2018.

[56] H. Han and K. A. Shore, "Zero crosstalk regime direct modulation of mutually coupled nanolasers," *IEEE Photonics J.*, vol. 9, pp. 1–2, 2017.

[57] S. Hachuda, S. Otsuka, S. Kita, et al., "Selective detection of sub-atto-molar streptavidin in 10^{13}-fold impure sample using photonic crystal nanolaser sensors," *Opt. Express*, vol. 21, pp. 12815–12821, 2013.

[58] S. Kita, K. Nozaki, S. Hachuda, et al., "Photonic crystal point-shift nanolasers with and without nanoslots—design, fabrication, lasing, and sensing characteristics," *IEEE J. Sel. Top. Quant. Electron.*, vol. 17, pp. 1632–1647, 2011.

[59] H. Abe, M. Narimatsu, T. Watanabe, et al., "Living-cell imaging using a photonic crystal nanolaser array," *Opt. Express*, vol. 23, pp. 17056–17066, 2015.

[60] J. Feng, W. Wen, X. Wei, et al., "Random organic nanolaser arrays for cryptographic primitives," *Adv. Mater.*, vol. 31, p. 1807880, 2019.

[61] S. Kita, K. Nozaki, and T. Baba, "Refractive index sensing utilizing a cw photonic crystal nanolaser and its array configuration," *Opt. Express*, vol. 16, pp. 8174–8180, 2008.

[62] J. J. Wu, H. Gao, R. Lai, et al., "Near-infrared organic single-crystal nanolaser arrays activated by excited-state intramolecular proton transfer," *Matter*, vol. 2, pp. 1233–1243, 2020.

[63] H. Kim, W. J. Lee, A. C. Farrell, et al., "Monolithic InGaAs nanowire array lasers on silicon-on-insulator operating at room temperature," *Nano Lett.*, vol. 17, pp. 3465–3470, 2017.

[64] H. Yan, R. He, J. Johnson, M. Law, R. J. Saykally, and P. Yang, "Dendritic nanowire ultraviolet laser array," *J. Am. Chem. Soc.*, vol. 125, pp. 4728–4729, 2003.

[65] T. Watanabe, H. Abe, Y. Nishijima, and T. Baba, "Array integration of thousands of photonic crystal nanolasers," *Appl. Phys. Lett.*, vol. 104, p. 121108, 2014.

[66] S. T. Ha, Y. H. Fu, N. K. Emani, et al., "Directional lasing in resonant semiconductor nanoantenna arrays," *Nat. Nanotechnol.*, vol. 13, pp. 1042–1047, 2018.

[67] A. Kodigala, T. Lepetit, Q. Gu, B. Bahari, Y. Fainman, and B. Kanté, "Lasing action from photonic bound states in continuum," *Nature*, vol. 541, p. 196, 2017.

[68] T. J. Lin, H. L. Chen, Y. F. Chen, and S. Cheng, "Room-temperature nanolaser from CdSe nanotubes embedded in anodic aluminum oxide nanocavity arrays," *Appl. Phys. Lett.*, vol. 93, p. 223903, 2008.

[69] K. Wang, Z. Gu, S. Liu, et al., "High-density and uniform lead halide perovskite nanolaser array on silicon," *J. Phys. Chem. Lett.*, vol. 7, pp. 2549–2555, 2016.

[70] D. Wang, A. Yang, W. Wang, et al., "Band-edge engineering for controlled multi-modal nanolasing in plasmonic superlattices," *Nat. Nanotechnol.*, vol. 12, p. 889, 2017.

[71] S. Pourjamal, T. K. Hakala, M. Nečada, et al., "Lasing in Ni nanodisk arrays," *ACS Nano*, vol. 13, pp. 5686–5692, 2019.

[72] W. Zhou, M. Dridi, J. Y. Suh, et al., "Lasing action in strongly coupled plasmonic nanocavity arrays," *Nat. Nanotechnol.*, vol. 8, p. 506, 2013.

[73] X. Meng, J. Liu, A. V. Kildishev, and V. M. Shalaev, "Highly directional spaser array for the red wavelength region," *Laser Photonics Rev.*, vol. 8, pp. 896–903, 2014.

[74] M. P. Knudson, R. Li, D. Wang, W. Wang, R. D. Schaller, and T. W. Odom, "Polarization-dependent lasing behavior from low-symmetry nanocavity arrays," *ACS Nano*, vol. 13, pp. 7435–7441, 2019.

[75] J. Y. Suh, C. H. Kim, W. Zhou, et al., "Plasmonic bowtie nanolaser arrays," *Nano Lett.*, vol. 12, pp. 5769–5774, 2012.

[76] F. van Beijnum, P. J. van Veldhoven, E. J. Geluk, M. J. de Dood, W. Gert, and M. P. van Exter, "Surface plasmon lasing observed in metal hole arrays," *Phys. Rev. Lett.*, vol. 110, p. 206802, 2013.

[77] C. Huang, W. Sun, Y. Fan, et al., "Formation of lead halide perovskite based plasmonic nanolasers and nanolaser arrays by tailoring the substrate," *ACS Nano*, vol. 12, pp. 3865–3874, 2018.

[78] Y. H. Chou, K. B. Hong, C. T. Chang, et al., "Ultracompact pseudowedge plasmonic lasers and laser arrays," *Nano Lett.*, vol. 18, pp. 747–753, 2018.

[79] H. Altug and J. Vučković, "Photonic crystal nanocavity array laser," *Opt. Express*, vol. 13, pp. 8819–8828, 2005.

[80] W. E. Hayenga, M. Parto, H. Hodaei, P. LiKamWa, D. N. Christodoulides, and M. Khajavikhan, "Coupled metallic nanolaser arrays," in *Conference on Lasers and Electro-Optics (CLEO)*, San Jose Optical Society of America (OSA), 2017, pp. 1–1, https://doi.org/10.1364/cleo_qels.2017.ftu3h.7.

[81] W. E. Hayenga, M. Parto, E. S. Cristobal, D. N. Christodoulides, and M. Khajavikhan, "Direct generation of structured light in

metallic nanolaser arrays," in *Conf. on Lasers and Electro-Optics (CLEO)* San Jose, Optical Society of America (OSA), 2018, pp. 1–2.

[82] M. Parto, W. Hayenga, D. N. Christodoulides, and M. Khajavikhan, "Mode-dependent coupling and vectorial optical vortices in metallic nanolaser arrays," in *Conf. on Lasers and Electro-Optics (CLEO)*, San Jose, Optical Society of America (OSA), 2019, FM1D-2.

[83] A. F. Koenderink, "Plasmon nanocavity array lasers: cooperating over losses and competing for gain," *ACS Nano*, vol. 13, pp. 7377–7382, 2019.

[84] M. B. Ross, C. A. Mirkin, and G. C. Schatz, "Optical properties of one-, two-, and three-dimensional arrays of plasmonic nanostructures," *J. Phys. Chem. C*, vol. 120, pp. 816–830, 2016.

[85] G. Cossu, A. M. Khalid, P. Choudhury, R. Corsini, and E. Ciaramella, "3.4 Gbit/s visible optical wireless transmission based on RGB LED," *Opt. Express*, vol. 20, pp. B501–B506, 2012.

[86] P. Xu, J. Gong, X. Guo, et al., "Fast lasing wavelength tuning in single nanowires," *Adv. Opt. Mater.*, vol. 7, p. 1900797, 2019.

[87] J. Cheng, C. L. Shieh, X. D. Huang, et al., "Efficient long wavelength AlGaInAs vertical-cavity surface-emitting lasers for coarse WDM applications over multimode fibre," *Electron. Lett.*, vol. 40, pp. 1184–1185, 2004.

[88] M. Lorke, T. Suhr, N. Gregersen, and J. Mørk, "Theory of nanolaser devices: rate equation analysis versus microscopic theory," *Phys. Rev. B*, vol. 87, no. 20, p. 205310, 28 May 2013.

[89] B. Bahari, L. Y. Hsu, S. H. Pan, et al., "Topological lasers generating and multiplexing topological light," arXiv preprint 1904.11873, 2019.

[90] Z. K. Shao, H. Z. Chen, S. Wang, et al., "A high-performance topological bulk laser based on band-inversion-induced reflection," *Nat. Nanotechnol.*, vol. 15, pp. 67–72, 2020.

[91] Z. Q. Yang, Z. K. Shao, H. Z. Chen, X. R. Mao, and R. M. Ma, "Spin-momentum-locked edge mode for topological vortex lasing," *Phys. Rev. Lett.*, vol. 125, p. 013903, 2020.

[92] Q. Zhan, "Cylindrical vector beams: from mathematical concepts to applications," *Adv. Opt. Photonics*, vol. 1, pp. 1–57, 2009.

[93] A. M. Yao and M. J. Padgett, "Orbital angular momentum: origins, behavior and applications," *Adv. Opt. Photonics*, vol. 3, pp. 161–204, 2011.

[94] S. Shahin, F. Vallini, F. Monifi, M. Rabinovich, and Y. Fainman, "Heteroclinic dynamics of coupled semiconductor lasers with optoelectronic feedback," *Opt. Lett.*, vol. 41, pp. 5238–5241, 2016.

[95] T. Suhr, P. T. Kristensen, and J. Mørk, "Phase-locking regimes of photonic crystal nanocavity laser arrays," *Appl. Phys. Lett.*, vol. 99, p. 251104, 2011.

[96] T. Y. Kao, J. L. Reno, and Q. Hu, "Phase-locked laser arrays through global antenna mutual coupling," *Nat. Photonics*, vol. 10, p. 541, 2016.

[97] J. S. Gongora, A. E. Miroshnichenko, Y. S. Kivshar, and A. Fratalocchi, "Anapole nanolasers for mode-locking and ultrafast pulse generation," *Nat. Commun.*, vol. 8, pp. 1–9, 2017.

[98] L. A. Coldren, S. W. Corzine, and M. L. Mashanovitch, *Diode Lasers and Photonic Integrated Circuits*, New Jersey: John Wiley & Sons, 2012.